Raman spectroscopy as a powerful tool to characterize ceria-based catalysts

S. Loridant

▶ **To cite this version:**

S. Loridant. Raman spectroscopy as a powerful tool to characterize ceria-based catalysts. Catalysis Today, 2021, 373, pp.98-111. 10.1016/j.cattod.2020.03.044 . hal-02990852

HAL Id: hal-02990852
https://hal.science/hal-02990852v1

Submitted on 17 Nov 2020

HAL is a multi-disciplinary open access archive for the deposit and dissemination of scientific research documents, whether they are published or not. The documents may come from teaching and research institutions in France or abroad, or from public or private research centers.

L'archive ouverte pluridisciplinaire **HAL**, est destinée au dépôt et à la diffusion de documents scientifiques de niveau recherche, publiés ou non, émanant des établissements d'enseignement et de recherche français ou étrangers, des laboratoires publics ou privés.

Raman spectroscopy as a powerful tool to characterize ceria-based catalysts

Stéphane Loridant[1,*]

[1] *Univ Lyon, Université Claude Bernard-Lyon 1, CNRS, IRCELYON-UMR 5256, 2 av. A. Einstein, F-69626 Villeurbanne Cedex, France*

* Corresponding Author: Ph. + 33 [0] 472 445 334, Fax + 33 [0] 472 445 399, E-mail: stephane.loridant@ircelyon.univ-lyon1.fr

Abstract

A review. CeO_2 is widely used and investigated as an oxide catalyst or support due to its unique redox property of oxygen storage and release. In this paper, the different opportunities offered by Raman spectroscopy for advanced characterization of ceria-based catalysts are reviewed: spectral modifications induced by nanocrystallinity, defects, doping and reduction, identification of supported molecular species, isolated atoms and nanoclusters, characterization of surface modes, hydroxyl groups, reaction intermediates such as peroxo and superoxo species. Finally, *in situ/operando* studies for environmental catalysis are summarized illustrating Raman spectroscopy as a powerful tool to characterize ceria-based catalysts.

Key Words: Raman spectroscopy, ceria, heterogeneous catalyst, nanomaterials, *in situ*, *operando*.

1. Introduction

CeO_2 is widely used as a catalyst or support component due to its unique redox property of oxygen storage and release [1]. Apart from its well-established application in three-way catalysis (TWC) [2], ceria is looming as a catalyst component for a wide range of catalytic applications [3] such as soot oxidation [4,5], NH_3-SCR reactions [6,7], remediation of volatile organic compounds (VOCs) [8], removal of CO_2, SO_2 and NOx gases [9], hydrogen purification and production processes [10], conversion of CO_2 [11], wet air oxidation [12] reforming of hydrocarbons and so on [1]. The shape and size modification, surface/face reconstruction, and faceting of ceria at the nanoscale level can offer an important tool to govern activity and stability in these reactions [13-18]. Furthermore, strong interaction between noble metals and ceria leads to their higher dispersion, electronic modifications and enhanced catalytic activity [19].

Raman spectroscopy is powerful for advanced structural characterization of heterogeneous catalysts all along their life cycle [20]. The different possibilities offered by this technique in the case of ceria-based catalysts are reviewed in this paper. In Part 2, Raman spectra of pure CeO_2 are described depending on its structural state (single crystal, nanocrystallized, nanostructured, reduced state). Then, spectral modifications induced by doping (Part 3) and observed for ceria-zirconia solutions (Part 4.1) are discussed. Characterization of catalysts such as noble metal oxides and vanadium oxide lying over ceria-based support allows unique distinguishing of different molecular species, nanoclusters and crystalline phases. This is highlighted in Parts 4.2 and 5.1, respectively. Finally, a selection of *in situ/operando* studies are summarized in Parts 5.2 and 5.3 to illustrate the wide panel of Raman spectroscopy.

2. Raman spectra of pure CeO_2

Raman spectroscopy provides identification of crystalline phases present in materials from the number of observed bands and their wavenumbers which are related to their space group and the bonds force constants, respectively. Usually, the Raman spectrum of a nanomaterial remains sufficiently similar to the corresponding single crystal one to allow univocal identification but as Raman spectroscopy is sensitive to the short-range order, to the chemical bond itself, spectral modifications (wavenumber, width, intensity) of disordered materials such as nanomaterials can be used to characterize them [21]. Therefore, Raman spectroscopy is widely used to characterize nanomaterials such as heterogeneous catalysts. In this part, spectral modifications observed for nanocrystallized CeO_2 are discussed regards the spectrum

of single crystal.

2.1 Single crystal

CeO_2 crystallizes in the cubic fluorite structure corresponding to the space group O_h^5 (Fm3m). Group theory predicts one triply degenerate Raman active optical phonon (F_{2g} symmetry) and one infrared-active optical phonon (F_{1u} symmetry), which presents either LO or TO character (with different wavenumbers) depending on the relative propagation/polarization directions of the mode [22]. The F_{2g} band located at 466 cm^{-1} at room temperature is often attributed for simplicity to symmetrical stretching vibration of the Ce–O8 units. In fact, it involves both Ce-O and O-O force constants, the O-O contribution being larger than the Ce-O stretching one [23]. Furthermore, the main band is quite intense because of high symmetry of the CeO_2 structure and of high polarizability of the Ce-O bonds. Therefore, characterization of ceria-based materials by Raman spectroscopy is very suitable. Furthermore, a weak band around 1180 cm^{-1} corresponds to the overtone of the LO mode (Raman inactive) located at 595 cm^{-1} and is therefore labelled 2LO [22,24]. The TO mode is located at 272 cm^{-1} [22,24].

Other second-order features at 264, 366, 550, 600, 676, 935 cm^{-1} were assigned to phonon overtones from the X and L points on the Brillouin-zone boundary on the basis of selection rules and using a rigid-ion model to determine the phonon dispersion curves [24]. Such curves were also obtained from DFT calculations achieved on a (4×4×4) primitive CeO_2 cell without strain [25,26] and as a function of positive and negative isotropic strain, which could be induced thermally or by cationic doping [25].

2.2 Nanocrystalline CeO_2

As shown in Figure 1a, decreasing the crystallite size of CeO_2 leads to broadening, asymmetry and red-shift of the F_{2g} band mostly below 50 nm [27-29]. Its half-width was shown to vary linearly with the inverse of crystallite size [28,29]. Broadening and asymmetry is due to reduction of the phonon lifetime according to the Phonon Confinement Model (PCM) [21,28-32]. The presence of defects also contributes to broadening [21,27-29,33] while the red-shift can be explained by strains due to the high curvature of nanocrystallites [27-29] and surface relaxation [34]. The lattice disorder was analysed from the shape of the Raman line using a spatial correlation model and calculating the phonon correlation length [21,28,29]. Typically, it was 10 nm for crystallites larger than 100 nm and decreased sharply below to reach 1 nm for crystallites of 4 nm (Figure 1b). Such large change in correlation

length was attributed to grain boundaries whose volume increases decreasing the crystallite size [21,28,29].

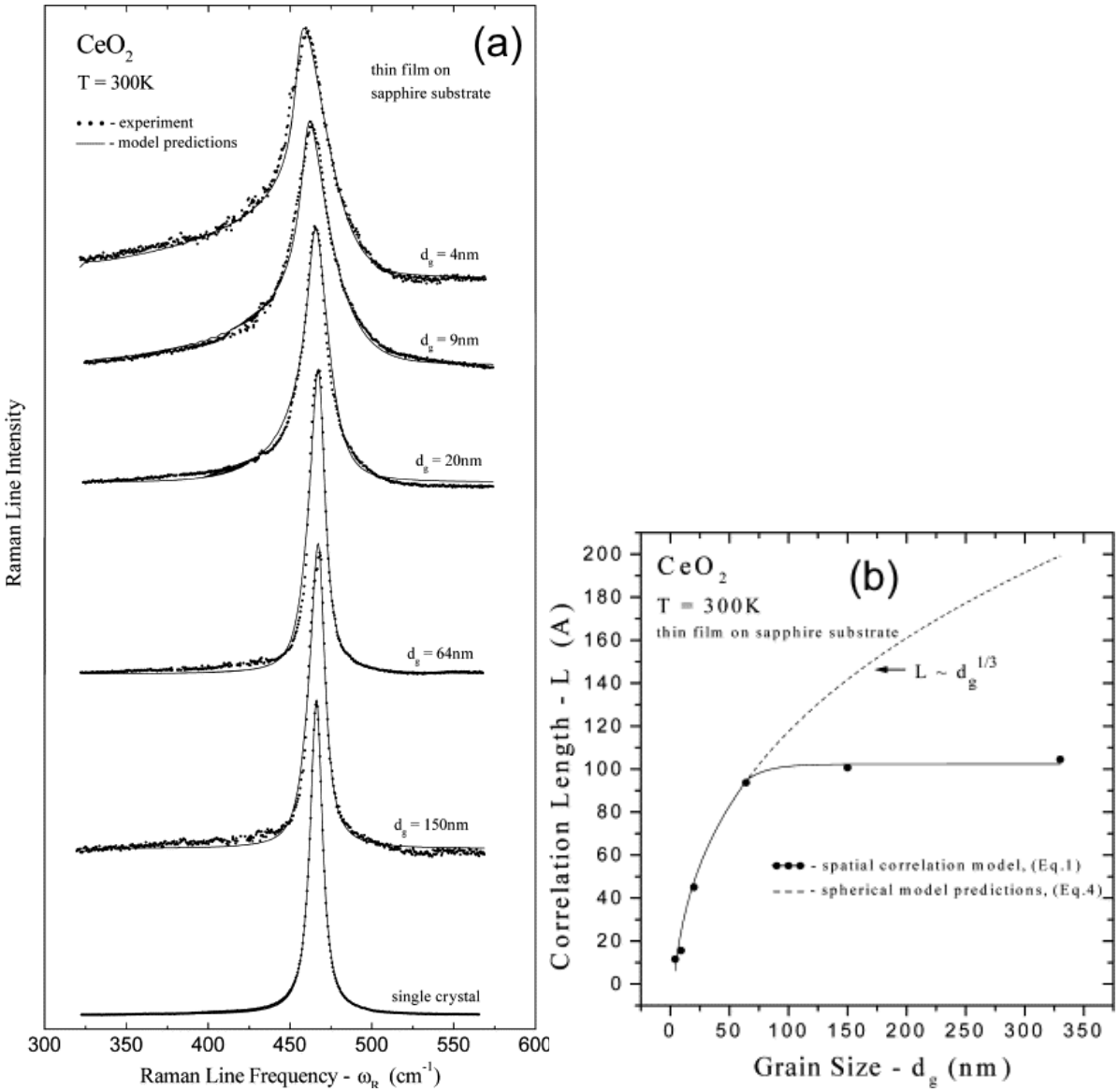

Figure 1. (a) Raman spectra of single crystal and nanocrystalline CeO_2 together with the curve fit according to the spatial correlation model (b) Correlation length as a function of crystallite size of nanocrystalline CeO_2 thin films. The dashed line is the correlation length estimated from a spherical model [28].

The temperature dependence of the F_{2g} Raman mode phonon wavenumber and broadening in CeO_2 nanocrystals was studied [35]. The phonon softening and phonon bandwidth were calculated using a model which considers the three-and four-phonon anharmonic processes. Note that an increase in the laser power leads to the same spectral evolutions by heating effect [36]. Furthermore, a reversible cubic (Fm-3m) to tetragonal (P42/nmc) phase transition was reported for nanosized (5-18 nm) ceria decreasing the

temperature from 75 to -25 °C while the lattice parameter was increased [37]. The electronic structures of these two phases are different: residual electrons are trapped in the oxygen vacancies for the tetragonal one whereas they occupy Ce f orbitals (presence of Ce^{3+} cations) for the cubic one. It led to observation of an additional band at 276 cm^{-1} which was attributed to the opposite vibrations of Ce and O atoms along c-axis which is Raman silent for the fluorite structure [37].

The broad band around 550-600 cm^{-1} observed in nanocrystallites is called 'the D-band' (D as Defects). Its location fits with second-order features (2TO (600 cm^{-1}) or 2LA (550 cm^{-1}) mode) according to the Weber's study [24] but such attribution has to be ruled out since it cannot explain its specific enhancement for nanocrystallites. Alternatively, it was attributed to the LO mode (F_{1u} symmetry, Raman inactive) arising from relaxation of selection rules [37,38] due to symmetry lowering induced by the presence of defects. Note that such defects could be Frenkel-type oxygen defects which were shown to be present in nanocrystalline CeO_2 [39,40]: an oxygen atom is then displaced from its lattice position to an interstitial site. Recently, DFT calculations on (2x2x2) cubic supercell containing 96 atoms ($Ce_{32}O_{64}$) with one $V_O^{\bullet\bullet}$ oxygen vacancy ($Ce_{32}O_{63}$) were undertaken [26]: one Raman band (first order) was calculated at 500 cm^{-1} for $Ce_{32}O_{63}$ cluster containing Ce^{3+} in direct proximity to the $V_O^{\bullet\bullet}$ defect and another one at 480 cm^{-1} when Ce^{3+} is located in the second coordination sphere of this defect. Therefore, the 550 cm^{-1} region was assigned to the $Ce^{3+}O_7V_O^{\bullet\bullet}$ coordination, whereas the 525 cm^{-1} region was attributed to the $Ce^{4+}O_7V_O^{\bullet\bullet}$ coordination [26]. Even if there is a significant shift between the calculated and the experimental values (the component near 600 cm^{-1} is not addressed) and even if Frenkel defects were not considered in this work, it should serve as reference in the future. Zhang

As illustrated by the comparison Raman spectra achieved at 514 and 364 nm in Figure 2b, the relative intensity of the D band is higher using ultraviolet (UV) excitation. In one hand, such feature can be interpreted by surface segregation of defects as UV excitation favours analysis of surface layers [42 and references therein]. As shown in Figure 2a, absorption due to the band gap of CeO_2 is much higher at 364 nm than at 514 nm. On the other hand, the high intensity of the 2 LO (1180 cm^{-1}) and 3 LO (1770 cm^{-1}) overtones was explained by resonance Raman effect which occurs when the wavelength of the laser exciting line is close to the one of an electronic transition [43] leading to multiphonon relaxation [42]. Hence, the D band could be enhanced either by a reduction of the penetration depth and a resonance effect using UV excitation.

UV Raman spectra achieved on nanoceria contained two D components at 590 and

560 cm^{-1}. The latter one enhanced after reduction à 500 °C was attributed to defect containing oxygen vacancies in agreement with the assignment from DFT calculations (see above and ref [26]). Upon O_2 consecutive adsorption at room temperature, the shoulder at 560 cm^{-1} disappears instantly and the D band shifts back to 590 cm^{-1} [39].

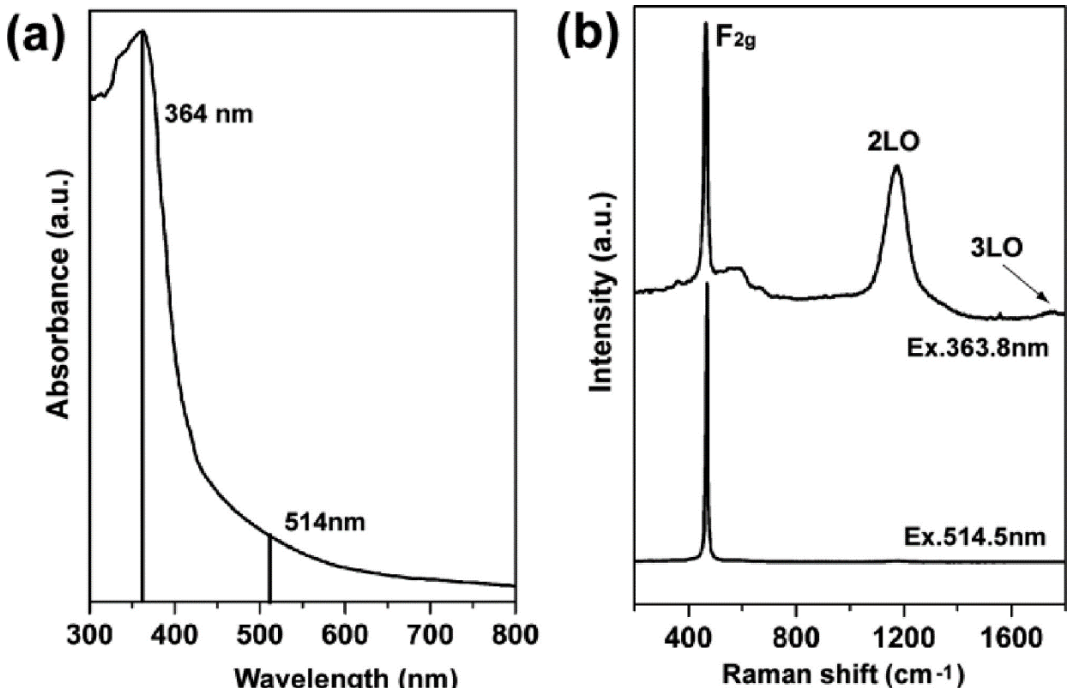

Figure 2. (a) Absorption spectrum and (b) UV/vis Raman spectra of ceria sample annealed at 1000 °C (crystallite size: 82.2 nm). Reprinted with permission from [42] Copyright 2009 American Chemical Society.

Another weak band observed around 250-260 cm^{-1} has been reported in several studies on nanocrystallized CeO_2 [39,44,45]. A relatively intense second order 2TA mode can be found in this spectral range according to the density of vibrational states (2w-DOS) [24,26]. However, such assignment has to be ruled out because the relative intensity of the band around 250-260 cm^{-1} strongly increases for small CeO_2 nanoparticles [26]. Convincingly, it was recently assigned from DFT calculations to a surface mode of the clean CeO_2 (111) surface as well as a shoulder at 400-405 cm^{-1} [26,33]. The two bands evolve synchronously upon reduction and reoxidation [46]. The former corresponds to the O−Ce longitudinal stretching of atoms in the outermost layers and the latter to a transversal Ce−O stretching vibration. It is worth mentioning that the two bands observed at 270 and 315 cm^{-1} for CeO_2 nanofilms were previously attributed to surface modes [47].

2.3 Nanostructured CeO_2

Raman spectra of various nanostructured CeO_2 were compared in several studies [39,48,49]. Their overall shape was similar but the F_{2g} band was broader and redshifted for nanorods compared to nanocubes and nanooctahedra in line with lower crystallinity.

Furthermore, the I_D/I_{F2g} ratio was higher for nanorods indicating higher proportion of defects [48,50]. Defect chemistry of nanoshaped ceria was investigated by UV Raman through the evolution of the D band under CO, H_2O and methanol. Oxygen vacancy ($V_O^{\bullet\bullet}$) defects were formed in CO at the expense of existing anion-Frenkel pair (O_i'') defects on cubes, whereas both defect types ($V_O^{\bullet\bullet}$ and O_i'') form on octahedra and rods [40]. Interestingly, the UV Raman spectra reported in this study contained shoulders at 404 and 487 cm^{-1} on both sides of the F_{2g} band which were explained by distortions in the fluorite structure.

2.4 Reduced CeO_2

Reduction of CeO_2 leads to formation of oxygen vacancies and Ce^{3+} cations (one for two). It leads to increase in the unit cell parameter, decrease in the bonds force constants leading to red-shift of the F_{2g} band. An example is provided in Part 5.3 (see Figure 11 and related comments). Oxygen vacancies formation can be followed by a red-shift of the D band due to an increase in the relative intensity of the component at 550 cm^{-1} compared to the one at 590 cm^{-1} [40,51]. At high reduction rate, Ce_2O_3 can be formed leading to observation of bands near 409, 189 and 103 cm^{-1} [26,52].

Furthermore, the presence of Ce^{3+} cations present in CeO_2 lattice can be evidenced using their electronic Raman scattering at 2100-2150 cm^{-1} associated to $^2F_{5/2} => {}^2F_{7/2}$ transition via a virtual state [46,53-55]. The direct transition can be observed by IR spectroscopy [53]. The Ce^{3+} Raman electronic spectrum depends on the crystal field which is different for $Ce_2Zr_2O_7$ pyrochlore, for instance: in this case, four bands are observed at 2147, 2492, 2556 and 2757 cm^{-1} [56].

Figure 3 compares the Raman spectra of Raman spectra of Pt/CeO_2 catalysts recorded in the 1900-2400 cm^{-1} spectral range upon redox sequences at 250 °C. The band typical of Ce^{3+} at 2130 cm^{-1} was observed only after the reduction steps for which the proportion of Ce^{3+} deduced from TPR measurements was 20% [46].

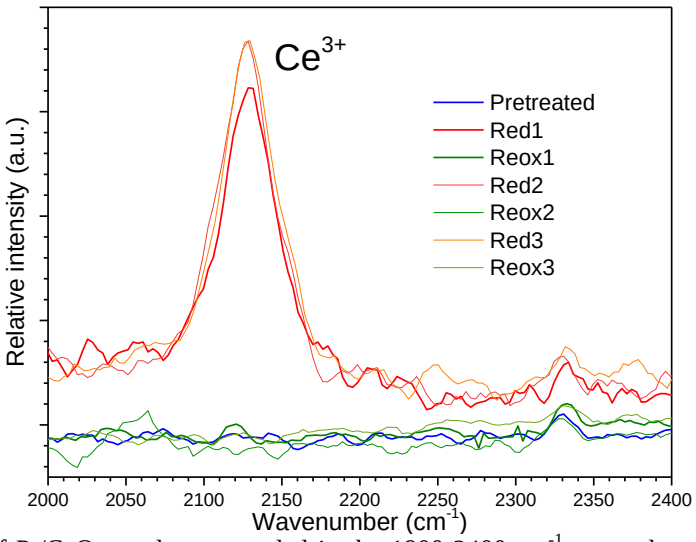

Figure 3. Raman spectra of Pt/CeO_2 catalysts recorded in the 1900-2400 cm^{-1} spectral ranges at RT after the initial oxidizing pre-treatment at 500 °C under 20% O_2 flow for 1 h and after successive reductions (Red1, 2 and 3) at 250 °C in H_2-N_2 and re-oxidations (Reox1, 2 and 3) at 250 °C in O_2-He.

2.5 OH groups

As by IR spectroscopy, the stretching vibrations of bridging and terminal OH surface groups of nanosized CeO_2 can be distinguished by Raman spectroscopy [44,45,57-59] depending on the ν(O-H) location. For instance, the band at 3716 cm^{-1} observed in Figure 4 is typical of terminal OH groups whereas the three ones at 3656, 3669 and 3691 cm^{-1} were attributed to bridging OH groups [60].

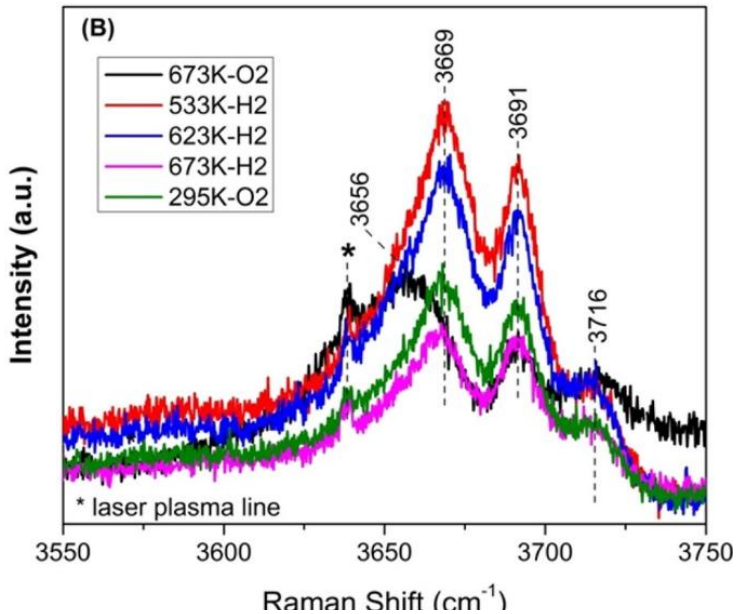

Figure 4. Raman spectra of CeO_2 collected at room temperature after calcination at 673 K, H_2 treatment at 533, 623, and 673 K, and exposure to O_2 at room temperature. The Raman peak marked with an asterisk (*) represents a laser plasma line and was used to normalize the Raman spectra intensity. Reprinted with permission from [60] Copyright 2017 American Chemical Society.

Upon H_2 treatment, an increase in the relative intensity of the band at 3691 cm^{-1} as well

as a blue shift of the bridging OH mode from 3656 to 3669 cm^{-1} with increased intensity revealed hydroxylation via H_2 dissociation on the ceria surface (Figure 4). The decrease of their intensities above 623 K was due to the removal of OH groups via water formation, i.e., formation of oxygen vacancies [60].

3. Doped ceria

Doping corresponds to incorporation of other elements into the ceria crystalline structure. Cations with lower valence than IV are usually added to generate oxygen vacancies and improve oxygen anion conductivity [1,4,5]. In this part, spectral modifications induced by such doping are discussed.

3.1 Characterization of the D defect band

The doping of fluorite CeO_2 by lower valence cations can be easily evidenced through the shift of its F_{2g} main band arising from modifications of Ce-O force constants. Furthermore, the intensity of the D defect band at 550-600 cm^{-1} increases with the doping rate which was early attributed to O vacancies generated by the doping from a model calculation using a Green's function [61]. A clear correlation between its relative intensity and $P(O_2)$ was established upon annealing of $Ce_{0.8}Sm_{0.2}O_{2-\delta}$ at 1000 °C [62]. In this work, two D components was distinguishable but not commented. Later, the D1 band located around 540–570 cm^{-1} whose relative intensity increases with the RE^{3+} rare earth doping rate has been assigned to extrinsic oxygen vacancies created into CeO_2 in order to maintain charge neutrality. On the other hand, the D2 band near 600 cm^{-1} has been attributed to the intrinsic $V_O^{\bullet\bullet}$ oxygen vacancies present in Ce^{3+}- $V_O^{\bullet\bullet}$ clusters because observed for pure nanocrystalline CeO_2 [63-66]. Corroboratively, the I_{D1}/I_{D2} ratio was shown to increase with the dopant content [67]. However, one can wonder why vibrations of Ce^{3+}- $V_O^{\bullet\bullet}$ clusters would be blue-shifted of 50 cm^{-1} compared to RE^{3+}- $V_O^{\bullet\bullet}$ clusters. Furthermore, two components can be distinguished between 550 and 600 cm^{-1} for pure nanocrystalline CeO_2 (see Part 2.2).

According to Nakajima et al. [68], the D1 band can be assigned to defect species including an oxygen vacancy that breaks the Oh symmetry and the D2 band to MO_8-type defect species with Oh symmetry including a dopant cation without any oxygen vacancy, respectively. Hence, the D1 and D2 bands were attributed to vibrations of clusters containing two Gd^{3+} cations and one oxygen vacancy and to GdO_8-type clusters without any oxygen vacancy, respectively [42]. These attributions of the D1 and D2 bands were later generalized for $Ce_{1-x}M_xO_{2-\delta}$ solid solutions (M = Gd, Zr, La, Sm, Y, Lu, and Pr) [69,70]. Note that one band near

600 cm^{-1} was observed for both M^{4+} (Zr) and M^{3+} (other elements) cations and was attributed in both cases to D2 defects [69]. In this study, dopants surface enrichment was evidenced comparing spectra recorded using 325 and 514 nm exciting lines [69]. More recently, the D1 and D2 bands were assigned on the basis of theoretical and experimental results, to stretching vibrations of O atoms between M^{3+} and Ce^{4+} ions near oxygen vacancy and to stretching vibrations of O atoms between M^{3+} or M^{4+} and Ce^{4+} ions without oxygen vacancy [71]. The attribution of the D1 band is in line with the one to $Ce^{3+}O_7V_O^{\bullet\bullet}$ coordination for undoped ceria (see Part 2.2 and [26]). However, the $Ce^{3+}O_8$ configuration was computed at lower wavenumber (480 cm^{-1}) than $Ce^{3+}O_7V_O^{\bullet}$ and $Ce^{4+}O_7V_O^{\bullet}$ configurations (500-550 cm^{-1}) in this study. Therefore, it appears that the attribution of the D2 band is still under debate.

Praseodymium doped ceria is a particular case since the relative intensity of the band at 570 cm^{-1} is high using a visible exciting line [64]. The observation of overtones and the fast change of relative intensity with excitation wavelength were explained by a resonance effect around 514 nm, which involved a Pr^{4+} containing defect stabilized at the oxidized state leading to an absorption band around 530 nm [72]. This defects band overlaps with the D1 and D2 bands (Figure 5). The reduction of Pr^{4+} cations contained in such defects modifies the electronic properties of praseodymium doped ceria inhibiting the resonance effect and leads to observation of D1 and D2 defects (Figure 5). Additionally, the number of D1 defects that involved Pr^{3+} or Ce^{3+} cations and oxygen vacancies increases allowing them to be distinguished.

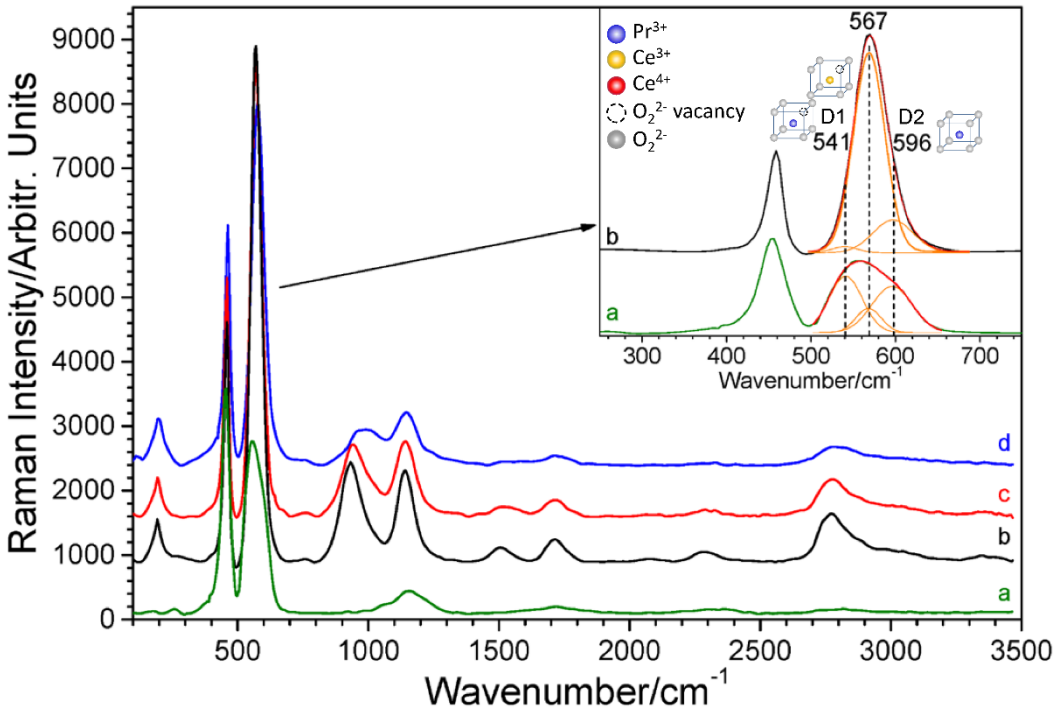

Figure 5. Raman spectra of $Ce_{0.8}Pr_{0.2}O_{2-\delta}$ recorded after reduction at 800 K for 60 min under 10% H_2 flow at (a)

77 K and after oxidation at 800 K for 30 min under 5% O_2 flow (b) at 77 K, (c) at 163 K, and (d) at 298 K using λ = 514 nm and P = 103 μW. The inset corresponds to a zoom of figures (a) and (b) between 300 and 700 cm^{-1} (adapted from [72]).

Finally, note that cerium is extracted from ores in which many other rare earth elements are present and the purification is not always very high. Hence, spectral features typical of doped ceria can be observed for undoped ceria containing rare earth impurities and the impurities level has to be considered when interpreting Raman spectra of undoped CeO_2.

3.2 Luminescence of rare earth dopants

One major limitation of Raman spectroscopy is superimposition of fluorescence phenomena hiding Raman bands because of much higher intensity. However, in case of rare earth dopants, fluorescence bands which correspond to electronic transitions involving 4f levels are thin and provide additional information when their positions are different from the Raman ones. The two types of bands can be distinguished by changing the exciting line as the relative wavenumber of Raman bands does not shift contrarily to the luminescence ones [73]. As Raman spectrometer covers usually a broad spectral range (several hundreds of nanometers), different fluorescence bands can be observed to determine the symmetry of cationic sites as with a spectrofluorometer. Decay times can be measured using pulsed laser with synchronous detection.

4. CeO_2 as catalyst support

As ceria-based support is nanocrystallized, all the features specific to nanocrystalline CeO_2 (see part 2.2) are observed for catalyst supported on CeO_2. Note that its cubic structure favours observation of vibrations of supported species especially because the single intense F_{2g} band is located at relatively low wavenumber. Sintering upon thermal treatment can be evidenced from decrease in bandwidth. Chemical evolution of CeO_2 support upon sulphidation is revealed from the S-O and S=O stretching vibrations observed in the 900-1400 cm^{-1} spectral range allowing identification of various surface oxysulfur species and bulk cerium-oxysulfur species [74,75]. Formation of $CePO_4$ in various phosphorus-contaminated automotive catalysts containing ceria as a washcoat component were observed using Raman spectroscopy [76]. UV Raman was particularly useful for detecting $CePO_4$ in customer-aged samples showing large fluorescent backgrounds under visible excitation.

Ceria-zirconia solid solutions are widely used in gas exhaust catalysts because improved thermal stability while also improving oxygen anionic mobility [1,2,4,5]. Noble

metals deposited on ceria-zirconia supports are widely used to catalyse oxidation and reduction reactions achieved in vehicle exhaust pipe for pollutants abatement. Therefore, Raman spectra of CeO_2-ZrO_2 solid solutions and supported noble metals are presented and discussed in the following.

4.1 CeO_2-ZrO_2 system

Raman spectroscopy has been also extensively used to distinguish polymorphs with subtle differences in O^{2-} atomic position in the CeO_2-ZrO_2 nano-oxide system [38,77-82]. The phase diagram of the $Ce_{1-x}Zr_xO_{2-y}$ mixed oxides is quite complex with three stable phases (monoclinic, tetragonal (t), and cubic) and two metastable tetragonal phases (t', t''). The space group of the later phases is P42/nmc with oxygen displacement in both cases while the c/a ratio is slightly higher than 1 for the t' phase and equal to 1 (pseudo cubic) for t" [79,82]. For large crystals (like in ceramics, for instance), the domain of stability at RT of t'' ranges in the zirconium poor region (typically 15%< x< 30%), the one of t' in a broad region (typically 30%< x< 85%) [79,82,83]. The phase transitions with composition and temperature were studied by Raman spectroscopy for samples calcined at high temperature such as ceramics [82,83]. It was also shown that thermal ''stability'' of the metastable phases depends strongly on particle size [79,81]. In fact, symmetry increases as crystallite size decreases because of disordering.

Considering group theory, only one vibrational mode is Raman active for the cubic phase (space group Fm3m) while the six Raman active modes are active for the tetragonal phases (space group P42/nmc). All the characteristic bands of tetragonal phase were observed for the t' phase but the ones below 400 cm^{-1} were not observed for the t'' phase in the case of large crystals [81,82]. Attribution to a given phase is harder for nanocrystallites because of bands broadening, activation of modes by zone folding and observation of defects modes (see part 2).

The evolutions of Raman spectra of $Ce_{(1-x)}Zr_xO_2$ solid solutions prepared by hydrothermal method followed by drying at 353 K overnight (as-prepared) and calcined at 1173 K for 4 h are plotted versus the x value in Figure 6a and b, respectively [84].

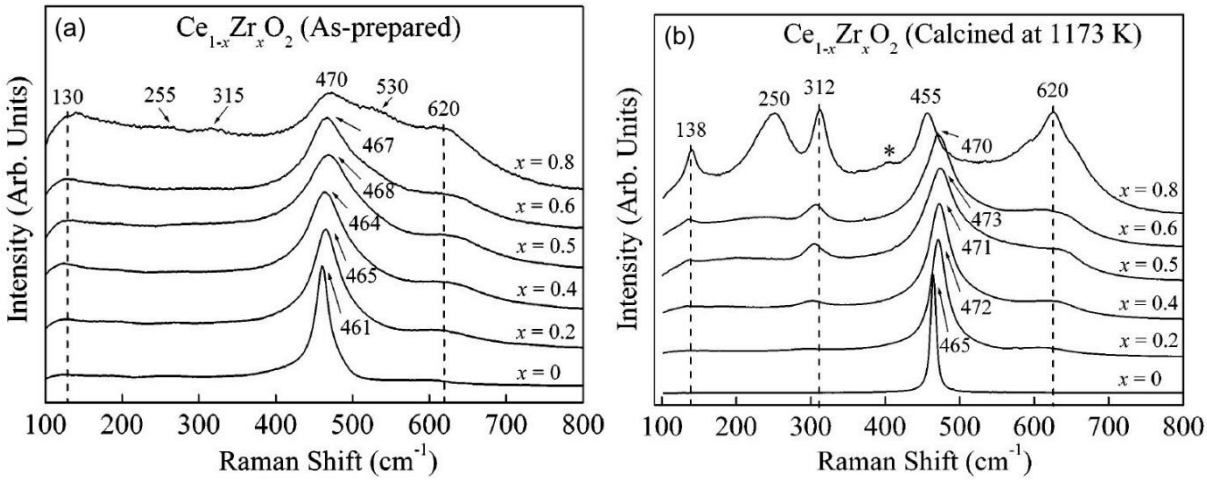

Figure 6. (a) Raman spectra of (a) as-prepared and (b) calcined at 1173 K $Ce_{(1-x)}Zr_xO_2$ (x = 0-0.8) samples. Reprinted with permission from [84] Copyright 2004 American Chemical Society.

Increasing the x value leads to a blue-shift (from 461 to 468 cm^{-1} for the as prepared samples and from 465 to 473 cm^{-1} for the calcined ones due to substitution of Ce^{4+} cations (ionic radius 0.97 Å) by smaller Zr^{4+} cations (ionic radius 0.84 Å) [85,86]. The associated band broadening reveals disorder induced by such substitution. The much larger width of the main band and its red-shift observed for the as prepared samples (x<0.8) indicates smaller crystallite size than for the calcined ones. Indeed, they ranged from 4.3 to 5.2 nm and from 14 to 48 nm, respectively. After calcination at 1173 K, no band was observed below 400 cm^{-1} for x=0.2 in agreement with the presence of t'' phase according to the phase diagram whereas the bands of tetragonal t' phase were observed for x ranging from 0.4 to 0.8. For the as prepared samples, no band was observed below 400 cm^{-1} for x<0.8. It can be due to either the decrease of crystallite size of t' phase or to stabilization of t'' phase. These two explanations show clearly that Raman spectra of nanosized $Ce_{1-x}Zr_xO_{2-y}$ mixed oxides has to be interpreted with care.

However, combined visible (non-resonant) and UV (resonant) Raman spectra were very useful in studying the structural properties of $Ce_{1-x}Zr_xO_2$ catalysis at the nanoscale because it provided detection selectivity in the tetragonal and cubic phases in CeO_2–ZrO_2 nanocrystals, respectively [87]. In particular, UV Raman spectra clearly evidenced the presence of a cubic phase containing Ce^{3+} cations in mixed oxide nanocrystals even in cases where they are characterized as the t' and t'' phase by XRD and visible-Raman spectroscopy. It was previously suggested from X-ray absorption spectra that the increase in the Ce^{3+} concentration with Zr^{4+} doping was due to larger ionic radius of Ce^{3+} (1.04 Å) than both Ce^{4+}(0.97 Å) and Zr^{4+}(0.84 Å) leading to decrease the total lattice-strain energy that accumulated due to the large interval between the ionic radii of Ce^{4+} and Zr^{4+} [88]. The anionic sublattice structure of

$Ce_{1-x}Zr_xO_{2-\delta}$ solids was also shown to depend on the preparation route by Raman spectroscopy [87]: for x = 0.5, the pseudo cubic t″ phase would be formed for the solid prepared by the citrate sol–gel method, while phase segregation (mixture of cubic, tetragonal phase) was proposed to occur for the corresponding material prepared by a coprecipitation with urea method [89]: a larger extent of defects and interstitial O atoms was evidenced for the materials prepared by the citrate sol–gel method. Furthermore, a novel approach based on sequential *in situ* Raman spectra under alternating oxidizing (20% O_2/He) and reducing (5% H_2/He) gas atmospheres showed that the D1 band above 600 cm^{-1} was selectively attenuated under reducing conditions at 450 °C for both undoped and rare earth doped solid solutions and was assigned to a metal–oxygen vibrational mode involving interstitial oxygen atoms that can be delivered under suitable conditions [89].

Finally, typical Raman spectra of κ and t* $CeZrO_4$ obtained from $Ce_2Zr_2O_{7+y}$ pyrochlore were also reported [90]: The spectrum of the κ phase contains bands near 171, 274, 306, 437, 475, 570, 602, 643 cm^{-1}. Their relative intensities vary depending on the local oxygen atom arrangements. The spectrum of t* $CeZrO_4$ is close to the one of the t' phase implying that the unit cells of t' and t* were essentially the same [90].

4.2 Supported noble metals

Raman spectroscopy also provides unique characterization of Pt-group noble metal oxides widely used in automobile exhaust catalysts since it allows to distinguish the different oxides and polymorphs even when supported at low loading [91,92]. For instance, segregated PdO can be easily evidenced by Raman spectroscopy from its strong B_{1g} mode at 650 cm^{-1} especially when using excitation near 514 nm leading to resonance effect [93,94]. Interestingly, difference of blue-shifts were explained by difference of strain due to encapsulation of PdO particles inside ceria-zirconia solid solutions [93].

Observation of a broad band around 700 cm^{-1} was early reported for noble metal oxides formed on CeO_2. It does not correspond to any crystalline phase as observed for $Rh_xCe_{1-x}O_{2-\delta}$ solid solutions calcined at 800 °C for which the shoulder at 650 cm^{-1} was related to the A_{1g} mode of α-Rh_2O_3 [95]. In fact, it has been associated with the capacity of ceria to form isolated M-O groups with Rh, Ir, Pd and Pt [95]. For Pt/CeO_2 and Pt/Al_2O_3-CeO_2, the two bands at 550 and 690 cm^{-1} were attributed to vibrations of bridging Pt-O-Ce groups at the Pt/CeO_2 interface [97]. They correspond to isolated Pt^{2+} cations (not a PtOx phase) in interaction with CeO_2 [46] and can maintain up to ca 150 °C under reducing conditions [98].

As shown in Figure 7, the higher the calcination temperature of 2%Pt/CeO_2 catalysts, the higher their disappearing temperature suggesting that Pt-O-Ce bond strength is stronger increasing the calcination temperature [99]. Their disappearing temperature was shown to depend on both the support ($Ce_{0.7}Zr_{0.3}O_2$ vs CeO_2) and the state of Pt (thermally stable single atoms vs nanoparticles) [100]. Similarly, the band at 670 cm^{-1} observed for iridium–ceria nanopowders synthesized by solution combustion was assigned to Ir-O-Ce stretching vibrations [101]. Note that the study of M-O-Ce bonds is particularly relevant in heterogeneous catalysis since they can be involved in Strong Metal Support Interaction (SMSI), in reduction process involved in formation of metal particles, in oxidation during their redispersion or even in a catalytic elementary step [46,97-100].

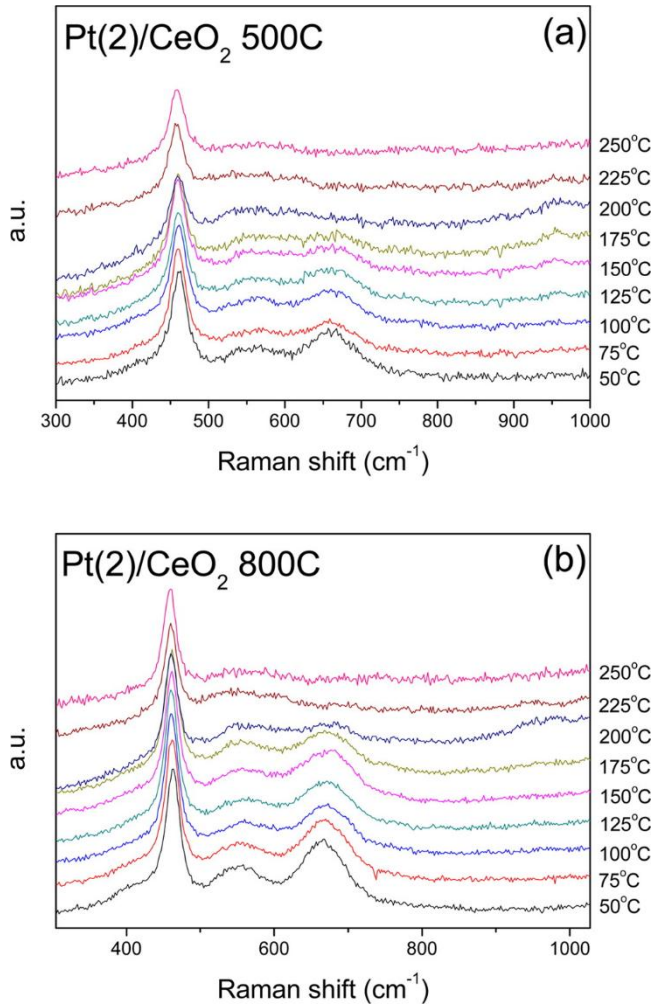

Figure 7. *In situ* Raman spectra of (a) 2 wt%Pt/CeO_2 calcined at 500 °C (labelled Pt(2)/CeO_2 500C) and (b) 2 wt%Pt/CeO_2 calcined at 800 °C (labelled Pt(2)/CeO_2 800C) recorded at temperature from 50 to 250 ° C with a temperature step of 25 °C, under 3% H_2/Ar. The parentheses value is the wt% of Pt in the sample. Each temperature was maintained for 20 min, and Raman spectra were obtained after cooling down to 50 °C. Reprinted with permission from [99] Copyright 2004 American Chemical Society.

Significant red-shift and broadening of the F_{2g} band of iridium-ceria [101] and nickel-ceria [102] catalysts synthesized by solution combustion and co-precipitation, respectively

were previously reported. In the study on iridium-ceria [101], broadening due to confinement effect in nano-particles was ruled out since the crystallite size determined from XRD analysis did not vary significantly with the Ir content and was rather high (30-50 nm). However, the red-shift was associated with a larger lattice parameter determined by XRD evidencing Ir incorporation into CeO_2 lattice and the broadening to disorder induced by this incorporation. Metal incorporation into the CeO_2 lattice can also be revealed through additional bands: for instance, a band at 187 cm^{-1} was assigned to the A_1 vibrations of Pd^{2+} ions in near square planar PdO_4 subunits with the C_{4v} symmetry in the lattice of the $Pd_xCe_{1-x}O_{2-x-\delta}$ solid solution [94]. Note that the band at 235-250 cm^{-1} observed in several of these studies [94,95,102] was tentatively attributed to the 2TA mode still according to the Weber's study (see part 2.2) [24].

5. *In situ/operando* studies

Raman spectroscopy is very valuable for *in situ* characterization of heterogeneous catalysts in gas and liquid phase. It is particularly true for reaction in aqueous phase since the Raman response of water is relatively weak by comparison with the IR one. Concerning gas phase reaction, the acquisition of Raman spectra up to typically 800 °C is possible using a green exciting line (most often used) because blackbody emission is low in the spectral range containing Raman bands [103]. *Operando* characterization corresponds to *in situ* spectra under true catalytic operation with on line activity measurements [104-112].

Raman scattering is an inherently low sensitivity process due to the small Raman cross-sections as compared to IR adsorption coefficients [113]. Therefore, Raman spectroscopy is most of the time used for structural characterization and observation of adsorbed species (intermediates or spectators) remains scarce compared to IR spectroscopy. When interpreting Raman spectra of ceria based catalysts, one should take into account the possible changes of absorption coefficient since ceria is a reductive oxide leading to UV-vis absorption and strong decrease in Raman bands intensity. An interesting wavelength-dependent absorption correction has been recently developped to take into account absorption effects [114].

In this part, a focus is made on *in situ* studies of vanadium oxide supported on CeO_2, identification of peroxo and superoxo species and finally different works concerning environmental catalysis are summarized.

5.1 vanadium oxide supported on CeO_2

As for numerous other supports, the effect of water vapour on the molecular structures of vanadium oxide supported on CeO_2 was early investigated by I.E. Wachs et al. Two bands of molecular vanadates were observed at the dehydrated state around 1020-1030 and 900-920 cm^{-1} and assigned to ν(V=O) and ν(V-O-V) stretching vibrations, respectively. The former is redshifted and broadened in the presence of water vapour because of hydrogen bonding between V=O groups and H_2O molecules [115]. In addition to structural information on molecular vanadates and determining the maximal coverage above which crystalline V_2O_5 is formed, Raman spectroscopy was used to follow $CeVO_4$ formed by interaction between vanadates and ceria during thermal treatments and reactions [83,116-121]. In the case of ceria-zirconia supports, polyvanadates were shown to interact preferentially with the CeO_2 portion of the mixed oxides and to form $CeVO_4$ at high temperature [122]. *Operando* studies during oxidative dehydrogenation of ethane suggested that the V-O-Ce bonds must be the sites involved in the rate-determining step [123,124]. Finally, the vanadia structures on different nanoshaped ceria were identified by *in situ* visible (633 nm) and UV (325 nm) Raman spectroscopy as a function of loading and calcination temperature [117,125]. It was found that both the surface structure and the amount of defect sites play major roles in the $CeVO_4$ formation. The easier formation of $CeVO_4$ on ceria rods, compared with cubes or octahedra was attributed to their lowest surface oxygen vacancy formation energy and largest amount of defect sites. As shown in the visible spectra of dehydrated VO_x/r-CeO_2 (CeO_2 nanorods) and VOx/c-CeO_2 (CeO_2 nanocubes) samples plotted in Figures 8A, the surface vanadia evolves from monomeric to polymeric VOx and to $CeVO_4$ crystalline phase as a function of VOx surface density. The main spectral differences between the two samples are the much weaker band of $CeVO_4$ at high VOx surface density on c-CeO_2 and the absence of bands attributed to V_2O_5. The ratio of the D to F_{2g} band (I_D/I_{F2g}) obtained from the UV spectra and representative of the relative amount of defect sites in ceria, are plotted in the insets of Figures 8B as a function of VOx surface density. It decreases continuously with increasing VOx loading for r-CeO_2 which implies that the surface VOx interacts closely with the defect sites in ceria rods. For c-CeO_2, the I_D/I_{F2g} ratio seems rather insensitive to the change in surface VOx density. This was attributed to the much larger particle size of c-CeO_2 than r-CeO_2. As Raman spectroscopy is a bulk technique, the I_D/IF_{2g} seems unaffected by anchorage of VOx on c-CeO_2 even though the surface/subsurface defect sites are consumed by interactions with VOx species [125].

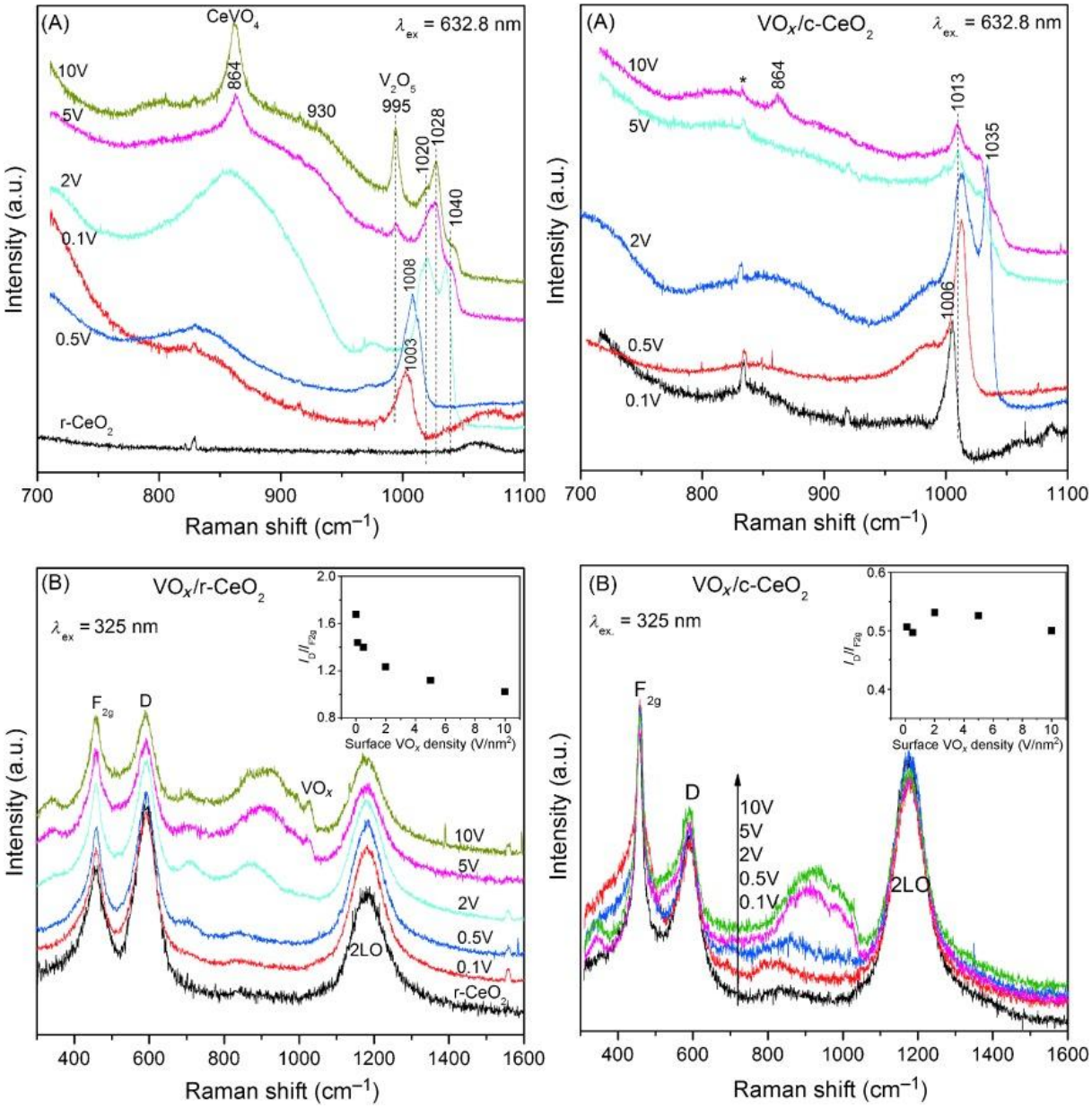

Figure 8. Visible (A) and UV (B) Raman spectra of dehydrated VOx/r-CeO_2 (CeO_2 nanorods) and VOx/c-CeO_2 (CeO_2 nanocubes) samples as a function of surface VOx density (V nm^{-2}). The inset in parts B is a plot of the ratio of I_D/I_{F2g} versus the surface VOx density. * indicates a plasma line from the laser. Reprinted with permission from [125] Copyright 2012 Wiley-VCH Verlag GmbH& Co. KGaA, Weinheim.

5.2 Peroxo and superoxo species

O_2^{2-} peroxo and O_2^- superoxo species are intermediates in the reoxidation sequence of reduced CeO_{2-x} to CeO_2:

$$O_2 \overset{e-}{\Rightarrow} O_2^- \overset{e-}{\Rightarrow} O_2^{2-} \Rightarrow 2O^- \overset{2e-}{\Longrightarrow} 2O^{2-}$$

Electrons consumed in this sequence are provided by Ce^{3+} cations leading to their reoxidation to Ce^{4+}. Raman spectroscopy is sensitive to probe peroxo and superoxo species formed upon oxygen adsorption on reduced ceria [39,44,45] because of the covalent character of their O=O bonds. The ν(O=O) stretching vibrations of peroxo and superoxo species are located in the

800-900 cm^{-1} and 1100-1200 cm^{-1} spectral range, respectively. Chimisorption experiments have to be achieved at very low laser power under microscope to avoid formation of oxygen species by photolysis [44]. Figure 9 compares the Raman spectra of pristine CeO_2 and 0.7% Pt/CeO_2 catalyst after reduction at 400, 450, and 500 °C recorded at low temperature (-100 °C) under O_2 flow. The three bands at 831-834 cm^{-1}, 854-862 cm^{-1} and 884-886 cm^{-1} correspond to ν(O-O) of peroxo species adsorbed on three different sites: the higher its wavenumber (the stronger the bond force constant) is, the more labile is. This trend was confirmed by TPO experiments followed by Raman spectroscopy [44]. The distributions of peroxo species adsorbed on defect sites of Pt/CeO_2 and CeO_2 were significantly different in spite of similar amounts: more labile species were formed during the reduction of 0.7% Pt/CeO_2 revealing that new sites were created during impregnation, calcination and/or reduction of Pt/CeO_2 compared to its bare support [44].

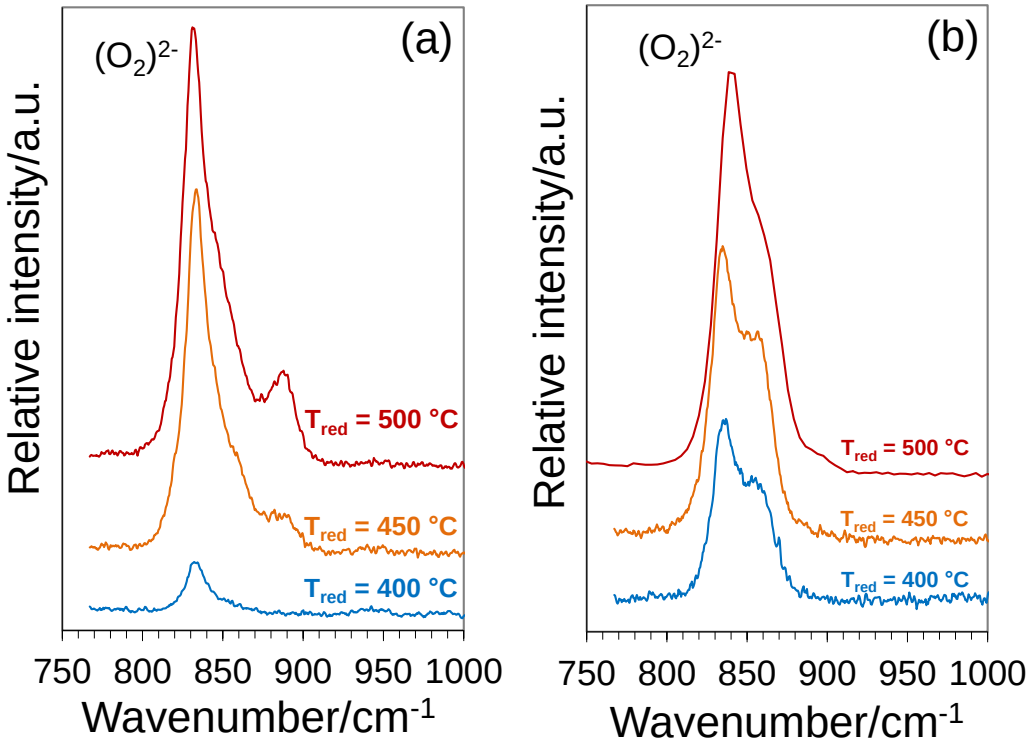

Figure 9. Comparison of the Raman spectra of pristine CeO_2 and 0.7% Pt/CeO_2 catalyst after reduction at 400, 450, and 500 °C recorded at -100 °C under O_2 flow.

Specific attribution to a given adsorption site has been sustained by DFT calculations [126-129]. In particular, the shape-dependence of O_2 adsorption and activation of ceria nanoparticles with (111) and (100) facets was investigated by *in situ* Raman spectroscopy and a facilitated formation of peroxide, superoxide, and weakly bound dioxygen species on the (100) facets was demonstrated [129].

5.3 Environmental catalysis

As peroxo and superoxo species are reoxidation intermediates (see part 6.2) as well as electrophilic species able to oxidize hydrocarbons, their observation by *in situ* and *operando* techniques is valuable when investigating environmental catalysis. For instance, consumption of peroxo species observed using operando Raman spectroscopy gave clear evidence for the participation of oxygen vacancies in CO oxidation over Au/ceria at room temperature [130]. In particular, two bands located at 847 and 881 cm^{-1} decreased during CO oxidation contrarily to the one at 830 cm^{-1}. As no dynamic of the band at 847 cm^{-1} was observed for bare ceria, it was associated with defects in the vicinity of the Au/CeO_2 interface whereas the band at 881 cm^{-1} was attributed to peroxo species directly located at the gold-ceria interface. The evolution of peroxo species along redox sequences achieved on Pt/CeO_2 was related to stabilisation of subnanometric Pt rafts leading to an outstanding low temperature catalytic activity for CO oxidation [46]. The relative intensity of peroxo oxygen species was maximal after reoxidation at room temperature suggesting that their dissociation into O^- and reduction to O^{2-} anions were limited at room temperature.

Operando Raman characterization of OH groups was particularly interesting in the study of the water-gas shift reaction over ceria-supported gold catalysts [131]. Indeed, the cleavage of O–H bonds is considered to be a key step in both the redox and associative mechanisms proposed in the literature. In this study, ^{18}O labelling of bare $CeO_2(111)$ and $Au/CeO_2(111)$ catalyst was achieved to gain insight into the mechanism of the WGS reaction, As shown in Figure 10, the hydroxyl bands at 3653 and 3682 cm^{-1} of bare CeO_2 shift by -10 and -12 cm^{-1}, respectively under both $H_2{}^{18}O/Ar$ and $CO/H_2{}^{18}O/Ar$ (left panel) contrarily to the corresponding unlabelled gas mixtures (right panel). This behavior coincides well with the estimated isotope factor based on isolated $^{16}O/^{18}O–^{1}H$ harmonic oscillators. Note that isotopic dilution ([H]/[D] < 10%) upon deuteration was would be useful to investigate hydroxyl groups dynamic since it suppresses the mechanical coupling and reduces strongly the bandwidth of ν(O-H) stretching bands as previously shown in different Raman studies [132,133].

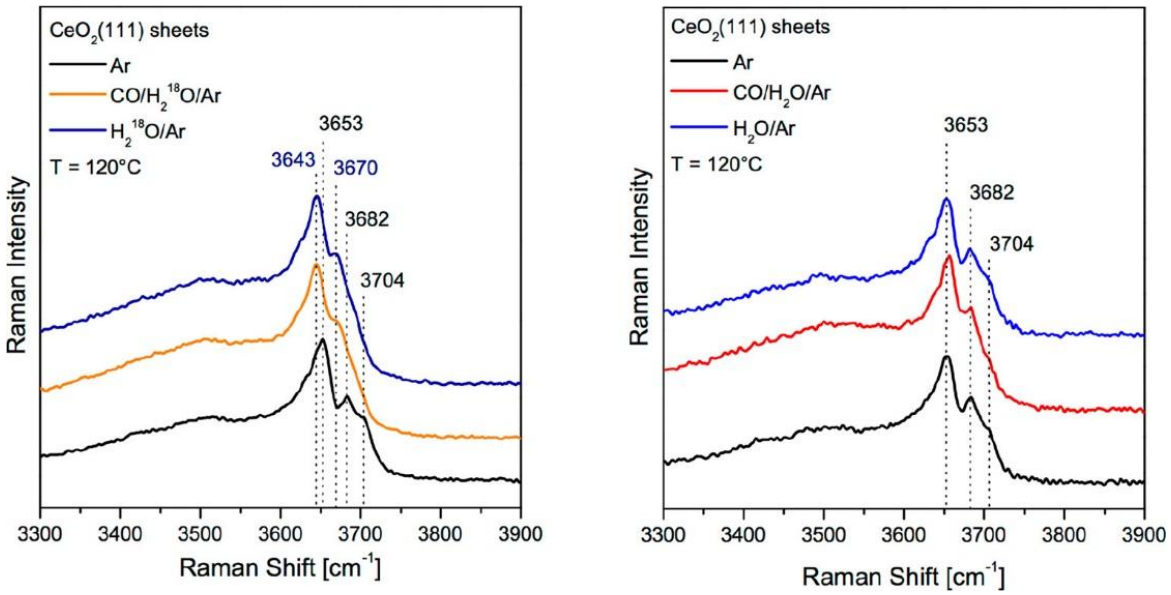

Figure 10. Raman spectra of bare CeO_2 at 120 °C during exposure to WGS reaction conditions (left panel: 2% CO, 8% $H_2{}^{18}O$, orange; right panel: 2% CO, 8% $H_2{}^{16}O$, red). For comparison, spectra in argon (black), in 8% $H_2{}^{18}O$ (dark blue left panel), and in 8% $H_2{}^{16}O$ (blue right panel) are shown. Spectra are offset for clarity. Reprinted with permission from [131] Copyright 2018 American Chemical Society.

No shift of the F_{2g} band was observed in bare ceria upon $^{16}O/^{18}O$ isotopic exchange indicating lattice oxygen (O^{2-}) was not liable to such exchange. Furthermore, as shown in Figure 11, the longitudinal and transversal stretching modes at 242 and 402 cm^{-1} probing the surface oxygen of the CeO_2(111) surface (see Part 2.2) disappeared in WGS reaction conditions but not under H_2O/Ar flow neither CO oxidation reaction conditions. The different red-shifts of the F_{2g} provided additional insight (see the different wavenumbers in Figure 11). In particular, it was attributed to reduction of the ceria subsurface under $CO/H_2{}^{18}O$/Ar at 120 °C and to large amounts of ^{18}O in the subsurface of the ceria support due to oxygen transfer from the surface to the ceria subsurface highlighting the oxygen dynamics of the ceria support.

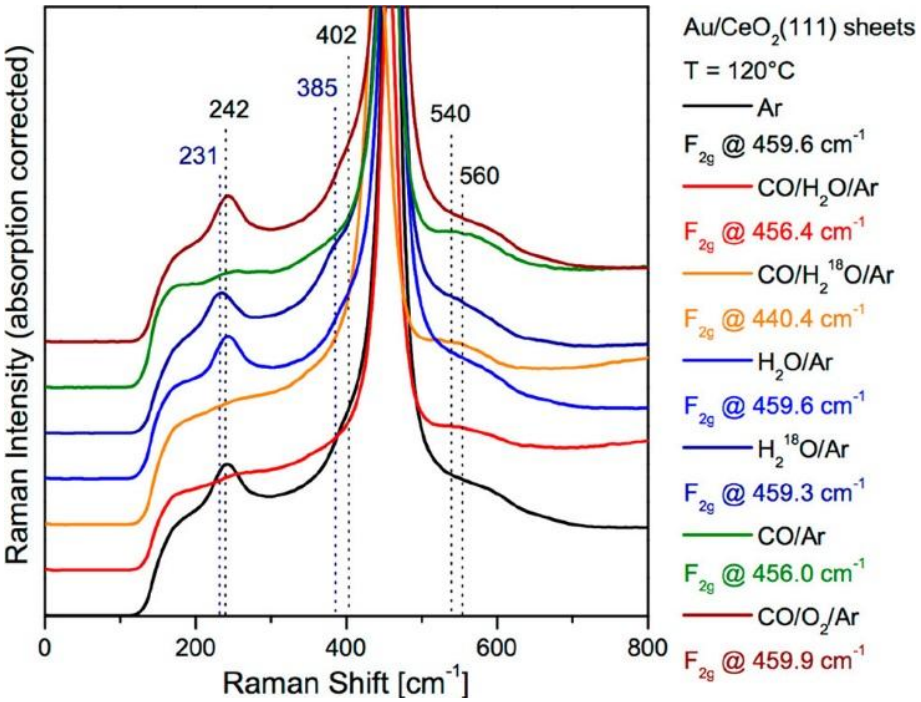

Figure 11. *In situ/operando* Raman spectra (phonon region) of 0.5 wt % Au/CeO_2 at 120 °C exposed to argon (black), WGS reaction conditions (2% CO, 8% $H_2{}^{16}O$, red), WGS reaction conditions (2% CO, 8% $H_2{}^{18}O$, orange), 10% $H_2{}^{16}O$ (blue), 8% $H_2{}^{18}O$, (dark blue), 2% CO (green), and CO oxidation reaction conditions (2% CO, 10% O_2, brown). Prior to all *in situ* measurements, the catalyst was equilibrated in argon at 120 °C. The F_{2g} band is cut off, and the position of the F_{2g} band is given at the right of the panel. Spectra are offset for clarity. Reprinted with permission from [131] Copyright 2018 American Chemical Society.

In situ Raman spectroscopy combined with quantitative FT-IR gas phase analysis was used to elucidate the mechanism of NO_2 storage in ceria [134,135]. As shown in Figure 12c, it allowed identification of nitrites (1292 cm^{-1}), free nitrates (726 and 1036 cm^{-1}), monodentate nitrates (1248 cm^{-1}), bidentate nitrates (1556-1605 cm^{-1}) and bridging nitrates (1622 cm^{-1}). Furthermore, a F_{2g} red shift of 1.5 cm^{-1} and an intensity loss (Figure 12a) were observed over the whole 60 min of NO_2 storage which is caused by formation of oxygen vacancies in the lattice. A similar temporal behavior was evidenced for the surface modes (bands at 250 and 407 cm^{-1}) describing a dependence of bulk defects on surface oxygen consumption. It was further concluded that the Ce-O surface sites play a key role for NOx storage, as their amount strongly influences the NOx storage capacity. Note that the ν(OH) band also decreased upon NO_2 exposure but faster: after 35 min no more hydroxides could be detected (see Fig. 12d), while surface oxygen was still observable (see Fig. 12b).

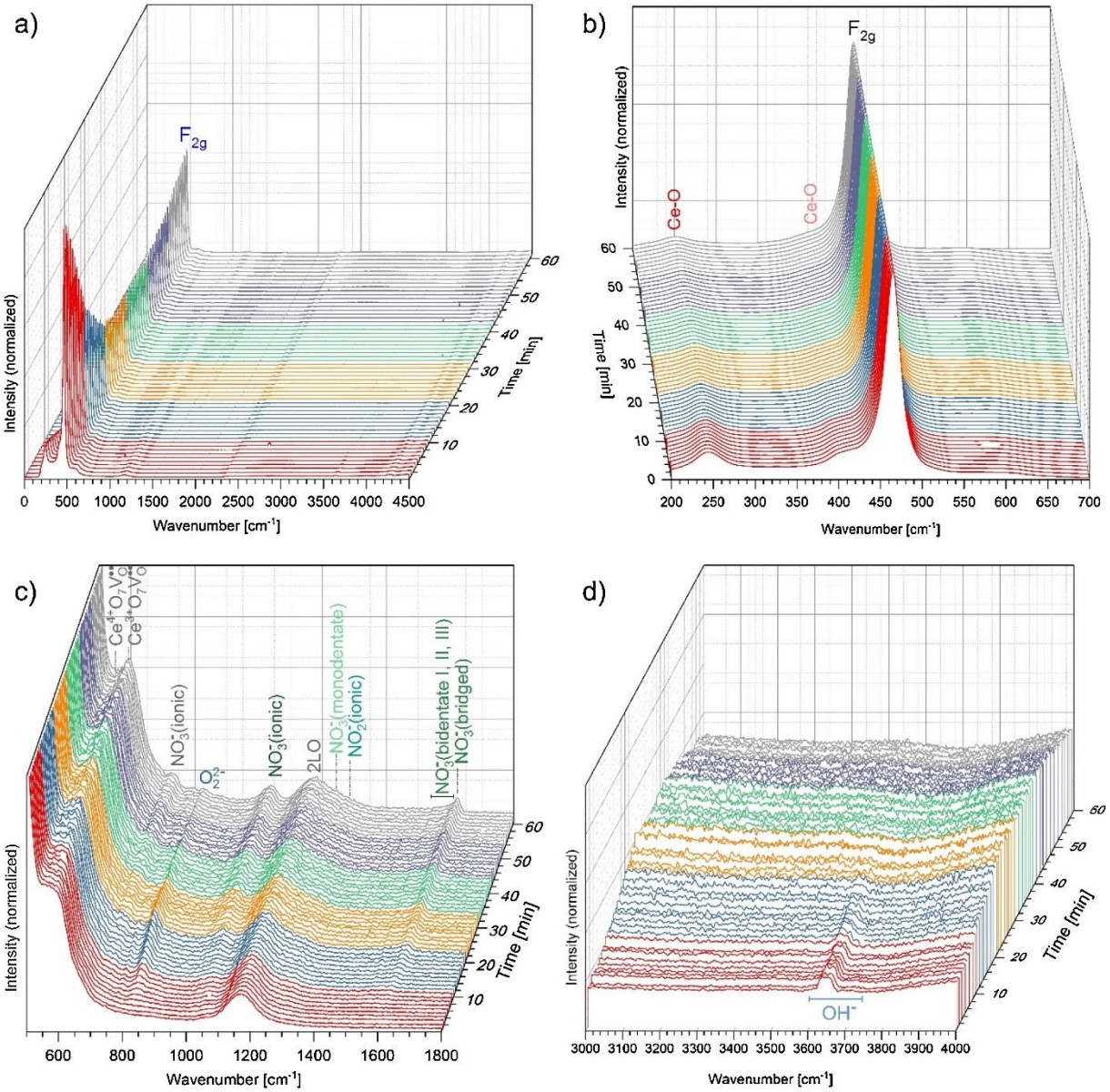

Figure 12. (a) *In situ* Raman spectra of oxidatively treated ceria showing the temporal evolution upon exposure to 500 ppm NO_2/20% O_2/N_2 at 30 °C. An enlarged view of the Raman spectra is shown for the regions (b) 200–700 cm^{-1}, (c) 500–1800 cm^{-1}, and (d) 3000–4000 cm^{-1} after normalization by the F_{2g} intensity to correct absorption effects. Reprinted with permission from [135] Copyright 2018 Elsevier B.V. All rights reserved.

6. Conclusions and perspectives

Considering the cubic fluorite structure of ceria, interpretation of its Raman spectra could be limited to the wavenumber, width and intensity of the F_{2g} band. However, more detailed structural properties can be obtained from small bands such as surface modes around 250 and 405 cm^{-1}, defect modes between 550 and 600 cm^{-1}, stretching vibrations of peroxo, superoxo and OH groups at 800-900, 1100-1200 cm^{-1} and 3600-3700 cm^{-1}, respectively as well as electronic Raman scattering of Ce^{3+} cations at 2130 cm^{-1}. In the case of catalysts supported over CeO_2, additional bands due to supported molecular species and crystalline phases can be

observed. Therefore, Raman spectroscopy is very powerful to investigate structural properties of ceria-based catalysts and has been widely used for *ex situ*, *in situ* and *operando* experiments which were reviewed in this paper. In the future, new field of investigation such as *in situ* Raman images to investigate structural evolutions [110,136-140], *in situ* Tip Enhanced Raman Spectroscopy (TERS) to reach high spatial resolution [141-144] and chemometric tools to extract subtle data [145-148] should be applied widening the field of Raman applications to ceria-based catalysts.

References

[1] P. Li, X. Chen, Y. Li, J.W. Schwank, A review on oxygen storage capacity of CeO_2-based materials: Influence factors, measurement techniques, and applications in reactions related to catalytic automotive emissions control, Catal. Today 327 (2019) 90-115.

[2] D. Devaiah, L.H. Reddy, S.-E. Park, B.M. Reddy, Ceria-zirconia mixed oxides: Synthetic methods and applications, Catal. Rev.: Sci. Eng. 60 (2018) 177-277.

[3] T. Montini, M. Melchionna, M. Monai, P. Fornasiero, Fundamentals and Catalytic Applications of CeO_2-Based Materials, Chem. Rev. 116 (2016) 5987-6041.

[4] D. Mukherjee, B.M. Reddy, Noble metal-free CeO_2-based mixed oxides for CO and soot oxidation, Catalysis Today 309 (2018), 309, 227-235.

[5] S. Liu, X. Wu, D. Weng, R. Ran, Ceria-based catalysts for soot oxidation: a review, J. Rare Earths 33 (2015) 567-590.

[6] J. Xu, H. Yu, C. Zhang, F. Guo, J. Xie, Development of cerium-based catalysts for selective catalytic reduction of nitrogen oxides: a review, New J. Chem. 43 (2019) 3996-4007.

[7] C. Tang, H. Zhang, L. Dong, Ceria-based catalysts for low-temperature selective catalytic reduction of NO with NH3, Catal. Sci. Tech. 6 (2016) 1248-1264.

[8] Q. Wang, K. L. Yeung, M. A. Banares, Ceria and its related materials for VOC catalytic combustion: A review, Catalysis Today (2019), Ahead of Print.

[9] U. Tumuluri, G. Rother, Z. Wu, Zili, Fundamental Understanding of the Interaction of Acid Gases with CeO_2: Surface Science to Practical Catalysis, Industrial & Engineering Chemistry Research 55 (2016) 3909-3919.

[10] A. Kubacka, A. Martinez-Arias, M. Fernandez-Garcia, Role of the Interface in Base-Metal Ceria-Based Catalysts for Hydrogen Purification and Production Processes, ChemCatChem 7 (2015) 3614-3624.

[11] F. Wang, M. Wei, D.G. Evans, X. Duan, CeO_2-based heterogeneous catalysts toward catalytic conversion of CO_2, J. Mater. Chem. A 4 (2016) 5773-5783.

[12] G. Lafaye, J. Barbier, D. Duprez, Impact of cerium-based support oxides in catalytic wet air oxidation: Conflicting role of redox and acid-base properties, Catal. Today 253 (2015) 89-98.

[13] A. Trovarelli, J. Llorca, Ceria Catalysts at Nanoscale: How Do Crystal Shapes Shape Catalysis? ACS Catal. 7 (2017) 4716-4735.

[14] M. Nolan, Surface effects in the reactivity of ceria: a first principles perspective, in: Z. Wu, S.H. Overbury (Eds), Catalysis by Materials with Well-Defined Structures, Elsevier, 2015, Chapter 6, pp159-192.

[15] A.K.P. Mann, Z. Wu, S.H. Overbury, The characterization and structure-dependent catalysis of ceria with well-defined facets, in: Z. Wu, S.H. Overbury (Eds), Catalysis by Materials with Well-Defined Structures, Elsevier, 2015, Chapter 3, pp71-97.

[16] S. Agarwal, B.L. Mojet, L. Lefferts, A.K. Datye, Ceria nanoshapes-structural and catalytic properties, in : Z. Wu, S.H. Overbury (Eds), Catalysis by Materials with Well-Defined Structures, Elsevier, 2015, Chapter 2, pp, 31-70.

[17] R.W. McCabe, A. Trovarelli, Forty years of catalysis by ceria: A success story, Applied Catalysis, B: Environmental 197 (2016) 1.

[18] M.V. Ganduglia-Pirovano, The non-innocent role of cerium oxide in heterogeneous catalysis: A theoretical perspective, Catal. Today 253 (2015) 20-32.

[19] M.S. Hegde, P. Bera, Noble metal ion substituted CeO_2 catalysts: Electronic interaction between noble metal ions and CeO_2 lattice, Catal. Today 253 (2015 40-50.

[20] S. Loridant, Raman Spectroscopy of Nanomaterials: Applications to Heterogeneous Catalysis, in O. S. Oluwafemi, S. Thomas, N. Kalarikkal, S. Mohan (Eds), Characterization of Nanomaterials: Advances and Key Technologies-Volume II, Elsevier, 2018, Chapter 2, pp37-59.

[21] G. Gouadec, P. Colomban, Raman Spectroscopy of nanomaterials: How spectra relate to disorder, particle size and mechanical properties, Progr. Cryst. Growth Charact. Mater. 53 (2007) 1-56.

[22] S. Mochizuki, infrared Optical Properties of Cerium Dioxide, Phys. Stat. Sol. 114 (1982) 189-199.

[23] T. Shimanouchi, M. Tsuboi, T.Miyazawa, Optically Active Lattice Vibrations as Treated by the GF-Matrix Method, J. Chem. Phys. 35 (1961) 1597-1612.

[24] W. Weber, K. Hass, J. McBride, Raman Study of CeO_2: Second-Order Scattering, Lattice Dynamics, and Particle-Size Effects, Phys. Rev. B: Condens. Matter Mater. Phys. 48 (1993) 178−185.

[25] J. Buckeridge, D.O. Scanlon, A. Walsh, C.R.A. Catlow, A.A. Sokol, Dynamical Response and Instability in Ceria under Lattice Expansion, Phys. Rev. B: Condens. Matter Mater. Phys. 87 (2013) 214304.

[26] C. Schilling, A. Hofmann, C. Hess, M.V. Ganduglia-Pirovano, Raman Spectra of Polycrystalline CeO_2: A Density Functional Theory Study, J. Phys. Chem. C 2017, 121, 20834−20849.

[27] J.E. Spanier, R.D. Robinson, F. Zhang, S.-W. Chan, I.P. Herman, Size-Dependent Properties of CeO_{2-y} Nanoparticles as Studied by Raman Scattering. Phys. Rev. B: Condens.

Matter Mater. Phys. 64 (2001) 245407.
[28] I. Kosacki, T. Suzuki, V Petrovsky, H. U. Anderson, P. Colomban, Lattice defects in nanocrystalline CeO_2 thin films, Radiation Effects & Defects in Solids 156 (2001) 109-115.
[29] I. Kosacki, T. Suzuki, H.U. Anderson, P. Colomban, Raman scattering and lattice defects in nanocrystalline CeO_2 thin films, Solid State Ionics 149 (2002) 99-105.
[30] H. Richter, Z.P. Wang, L. Ley, The one phonon spectrum in microcrystalline silicon, Solid State Commun. 39 (1981) 625-629.
[31] Z.V. Popovic, Z. Dohcevic-Mitrovic, M.J. Konstantinovic, M. Scepanovic, Raman scattering characterization of nanopowders and nanowires (rods), J. Raman Spectrosc. 38 (2007) 750-755.
[32] M. Grujic-Brojcin, M.J. Scepanovic, Z.D. Dohcevic-Mitrovic, Z.V. Popovic, Use of phonon confinement model in simulation of Raman spectra of nanostructured materials, Acta Phys. Pol. A 116 (2009), 51-54.
[33] A. Filtschew, K. Hofmann, C. Hess, Ceria and Its Defect Structure: New Insights from a Combined Spectroscopic Approach, J. Phys. Chem. C 120 (2016) 6694-6703.
[34] C.C. Yang, S. Li, Size-Dependent Raman Red Shifts of Semiconductor Nanocrystals, J. Phys. Chem. B 112 (2008) 14193-14197.
[35] Z.V. Popovic, Z. Dohcevic-Mitrovic, A. Cros, A. Cantarero, Raman scattering study of the anharmonic effects in CeO_{2-y} nanocrystals, J. Phys.: Condens. Matter 19 (2007) 496209/1-496209/9.
[36] A.C. Oliveira, A.N. da Silva, J.A.L. Junior, P.T.C. Freire, A.C. Oliveira, J.M. Filho, Structural changes in nanostructured catalytic oxides monitored by Raman spectroscopy: Effect of the laser heating, J. Phys. Chem. Solids 102 (2017) 90-98.
[37] H. Zhu, C. Yang, Q. Li, Y. Ren, J.C. Neuefeind, L. Gu, H. Liu, L. Fan, J. Chen, J. Deng, N. Wang, J. Hong, X. Xing, Charge transfer drives anomalous phase transition in ceria, Nat. Commun. 9 (2018) 1-8.
[38] B.M. Reddy, P. Lakshmanan, A. Khan, S. Loridant, C. Lopez-Cartes, T.C. Rojas, A. Fernandez, Surface Stabilized Nanosized $Ce_xZr_{1-x}O_2$ Solid Solutions over SiO_2: Characterization by XRD, Raman, and HREM Techniques, J. Phys. Chem. B 109 (2005) 13545-13552.
[39] Z. Wu, M. Li, J. Howe, H.M. Meyer III, S.H. Overbury, Probing Defect Sites on CeO_2 Nanocrystals with Well-Defined Surface Planes by Raman Spectroscopy and O_2 Adsorption, Langmuir 26 (2010) 16595–16606.
[40] S. Agarwal, X. Zhu, E. J. M. Hensen, B. L. Mojet and L. Lefferts, Surface-Dependence

of Defect Chemistry of Nanostructured Ceria, J. Phys. Chem. C 119 (2015) 12423–12433.
[41] C. Paun, O.V. Safonova, J. Szlachetko, P.M. Abdala, M. Nachtegaal, J. Sa, E. Kleymenov, A. Cervellino, F. Krumeich, J.A. van Bokhoven, Polyhedral CeO_2 Nanoparticles: Size-Dependent Geometrical and Electronic Structure, J. Phys. Chem. C 2012, 116, 7312−7317.
[42] T. Taniguchi, T. Watanabe, N. Sugiyama, A.K. Subramani, H. Wagata, N. Matsushita, M. Yoshimura, Identifying Defects in Ceria-Based Nanocrystals by UV Resonance Raman Spectroscopy. J. Phys. Chem. C 113 (2009) 19789−19793.
[43] P.C. Stair, The Application of UV Raman Spectroscopy for the Characterization of Catalysts and Catalytic Reactions, Adv. Catal. 51 (2007) 75-98.
[44] M. Daniel, S. Loridant, Probing reoxidation sites by *in situ* Raman spectroscopy: differences between reduced CeO_2 and Pt/CeO_2, J. Raman Spectrosc. 43 (2012) 1312-1319.
[45] V.V. Pushkarev, V.I. Kovalchuk, J.L. d'Itri, Probing Defect Sites on the CeO_2 Surface with Dioxygen. J. Phys. Chem. B 108 (2004) 5341−5348.
[46] G. Ferré, L. Burel, M. Aouine, F. Bosselet, S. Ntais, T. Epicier, F.J. Cadete Santos Aires, C. Geantet, A. Gaenzler, F. Maurer, M. Casapu, J.-D. Grunwaldt, S. Loridant, P. Vernoux, Exploiting the dynamic properties of Pt on ceria for low temperature CO oxidation, Appl. Catal. B, submitted.
[47] S. Wang, W. Wang, J. Zuo, Y. Qian, Study of the Raman spectrum of CeO_2 nanometer thin films, Mater. Chem. Phys. 68 (2001) 246-248.
[48] S. Agarwal, L. Lefferts, B.L. Mojet, Ceria Nanocatalysts: Shape Dependent Reactivity and Formation of OH, ChemCatChem 5 (2013) 479-489.
[49] I. Trenque, G.C. Magnano, M.A. Bolzinger, L. Roiban, F. Chaput, I. Pitault, S. Briançon, T. Deverse, K. Masenelli-Varlot, M. Bugnet D. Amans, Shape-selective synthesis of nanoceria for degradation of paraoxon as chemical warfare simulant, Phys. Chem. Chem. Phys. 21(2019) 5455-5465.
[50] Q. Dai, H. Huang, Y. Zhu, W. Deng, S. Bai, X. Wang, G. Lu, Catalysis oxidation of 1,2-dichloroethane and ethyl acetate over ceria nanocrystals with well-defined crystal planes, Appl. Catal.B: Environmental 117-118 (2012) 360-368.
[51] F. Vindigni, M. Floriana, D. Maela, T. Alessandro, T. Tabakova, A. Zecchina, Surface and Inner Defects in Au/CeO_2 WGS Catalysts: Relation between Raman Properties, Reactivity and Morphology, Chem. Eur. J. 17 (2011) 4356-4361.
[52] D. Avisar, T. Livneh, The Raman-Scattering of A-Type Ce_2O_3, Vib. Spectrosc. 86 (2016) 14−16.

[53] V.M. Orera, R.I. Merino and F. Pena, $Ce^{3+} \leftrightarrow Ce^{4+}$ conversion in ceria-doped zirconia single crystals induced by oxido-reduction treatments, Solid State Ion. 72 (1994) 224-231.

[54] S. Urban, I. Djerdj, P. Dolcet, L. Chen, M. Möller, O. Khalid, H. Camuka, R. Ellinghaus, C. Li, S. Gross, P.J. Klar, B. Smarsly, H. Over, *In Situ* Study of the Oxygen-Induced Transformation of Pyrochlore $Ce_2Zr_2O_{7+x}$ to the $\kappa^-Ce_2Zr_2O_8$ Phase, Chem. Mater. 29 (2017) 9218-9226.

[55] T. Otake, H. Yugami, H. Naito, K. Kawamura, T. Kawada, J. Mizusaki, Ce^{3+} concentration in ZrO_2-CeO_2-Y_2O_3 system studied by electronic Raman scattering, Solid State Ion. 135 (2000) 663-667.

[56] P.B. Oliete, A. Orera, M. L. Sanjuán, Spectroscopic insight into the interplay between structural disorder and oxidation degree in melt- grown $Ce_{0.5}Zr_{0.5}O_{2-y}$ compounds, J. Raman Spectrosc. (2020) 1–14.

[57] C. Binet, A. Badri, J.-C. Lavalley, A Spectroscopic Characterization of the Reduction of Ceria from Electronic Transitions of Intrinsic Point Defects, J. Phys. Chem. 98 (1994) 6392-6398.

[58] A. Badri, C. Binet, J.-C. Lavalley, An FTIR study of surface ceria hydroxy groups during a redox process with H_2, J. Chem. Soc., Faraday Trans. 92 (1996) 4669-4673.

[59] C.T. Nottbohm, C. Hess, Investigation of ceria by combined Raman, UV-vis and X-ray photoelectron spectroscopy, Catal. Commun. 22 (2012) 39-42.

[60] Z. Wu, Y. Cheng, F. Tao, L. Daemen, G.S. Foo, L. Nguyen, X. Zhang, A. Beste, A.J. Ramirez-Cuesta, Direct Neutron Spectroscopy Observation of Cerium Hydride Species on a Cerium Oxide Catalyst, J. Am. Chem. Soc. 139 (2017) 9721-9727.

[61] J.R. McBride, K.C. Hass, B.D. Poindexter, W.H. Weber, Raman and X-ray studies of $Ce_{1-x}RE_xO_{2-y}$, where RE=La, Pr, Nd, Eu, Gd, and Tb, J. Appl. Phys. 76 (1994) 2435-2441.

[62] A. Mineshige, T. Taji, Y. Muroi, M. Kobune, S. Fujii, N. Nishi, M. Inaba, Z. Ogumi, Oxygen chemical potential variation in ceria-based solid oxide fuel cells determined by Raman spectroscopy, Solid State Ion. 135 (2000) 481-485.

[63] Z.D. Dohcevic-Mitrovic, M. Grujic-Brojcin, M. Scepanovic, Z.V. Popovic, S. Boskovic, B. Matovic, M. Zinkevich, F. Aldinger, $Ce_{1-x}Y(Nd)_xO_{2-\delta}$ nanopowders: potential materials for intermediate temperature solid oxide fuel cells, J. Phys.: Condens. Matter 18 (2006) S2061-S2068.

[64] M. Guo, J. Lu, Y. Wu, Y. Wang, M. Luo, UV and Visible Raman Studies of Oxygen Vacancies in Rare-Earth-Doped Ceria, Langmuir 27 (2011) 3872-3877.

[65] N. Paunovic, Z. Dohcevic-Mitrovic, R. Scurtu, S. Askrabic, M. Prekajski, B. Matovic,

Z.V. Popovic, Suppression of inherent ferromagnetism in Pr-doped CeO_2 nanocrystals, Nanoscale 4 (2012) 5469-5476.

[66] W. Lee, S.-Y. Chen, Y.-S. Chen, C.-L. Dong, H.-J. Lin, C.-T. Chen, A. Gloter, Defect Structure Guided Room Temperature Ferromagnetism of Y‑Doped CeO_2 Nanoparticles, J. Phys. Chem. C 118 (2014) 26359-26367.

[67] W. Lee, S.-Y. Chen, E. Tseng, A. Gloter, C.-L. Chen, Study of Defect Structure in Ferromagnetic Nanocrystalline CeO_2: Effect of Ionic Radius, J. Phys. Chem. C 120 (2016) 14874−14882.

[68] A. Nakajima, A. Yoshihara, M. Ishigame, Defect-induced Raman spectra in doped CeO_2, Phys. Rev. B: Condens. Matter Mater. Phys. 50 (1994) 13297−13307.

[69] L. Li, F. Chen, J.-Q Lu, M.-F. Luo, Study of Defect Sites in $Ce_{1-x}MO_{2-\delta}$ (x = 0.2) Solid Solutions Using Raman Spectroscopy, J. Phys. Chem. A 115 (2011) 7972-7977.

[70] D. Avram, M. Sanchez-Dominguez, B. Cojocaru, M. Florea, V. Parvulescu, C. Tiseanu, Toward a Unified Description of Luminescence-Local Structure Correlation in Ln Doped CeO_2 Nanoparticles: Roles of Ln Ionic Radius, Ln Concentration, and Oxygen Vacancies, J. Phys. Chem. C 119 (2015) 16303-16313.

[71] Y. Xu, F. Wang, X. Liu, Y. Liu, M. Luo, B. Teng, M. Fan, X. Liu, Resolving a Decade-Long Question of Oxygen Defects in Raman Spectra of Ceria-Based Catalysts at Atomic Level, J. Phys. Chem. C, doi.org/10.1021/acs.jpcc.9b00633.

[72] A. Westermann, C. Geantet, P. Vernoux, S. Loridant, Defects band enhanced by resonance Raman effect in praseodymium doped CeO_2, J. Raman Spectrosc. 47 (2016) 1276-1279.

[73] P. Fornasiero, A. Speghini, R. Di Monte, M. Bettinelli, J. Kaspar, A. Bigotto, V. Sergo, M. Graziani, Laser-Excited Luminescence of Trivalent Lanthanide Impurities and Local Structure in CeO_2-ZrO_2 Mixed Oxides, Chem. Mater. 16 (2004) 1938-1944.

[74] J. Twu, C.J. Chuang, K.I. Chang, C.H. Yang, K.H. Chen, Raman spectroscopic studies on the sulfation of cerium oxide, Appl. Catal. B: Environmental 12 (1997) 309-324.

[75] R. Flouty, E. Abi-Aad, S. Siffert, A. Aboukais, Formation of cereous sulphate phase upon interaction of SO_2 with ceria at room temperature, J. Therm. Anal. Calorim. 73 (2003) 727-734.

[76] D. Uy, A.E. O'Neill, L. Xu, W.H. Weber, R.W. McCabe, Observation of cerium phosphate in aged automotive catalysts using Raman spectroscopy, Appl. Catal. B: Environmental 41 (2003) 269-278.

[77] B.M. Reddy, A. Khan, P. Lakshmanan, M. Aouine, S. Loridant, J.-C. Volta, Structural

Characterization of Nanosized CeO_2-SiO_2, CeO_2-TiO_2, and CeO_2-ZrO_2 Catalysts by XRD, Raman, and HREM Techniques, J. Phys. Chem. B 109 (2005) 3355-3363.

[78] B.M. Reddy, A. Khan, Y. Yamada, T. Kobayashi, S. Loridant, J.-C. Volta, Structural Characterization of CeO_2-MO_2 (M=Si^{4+}, Ti^{4+}, and Zr^{4+}) Mixed Oxides by Raman Spectroscopy, X-ray Photoelectron Spectroscopy, and Other Techniques, J. Phys. Chem. B 107 (2003) 11475-11484.

[79] R. Di Monte, J. Kaspar, Nanostructured CeO_2–ZrO_2 mixed oxides, J. Mater. Chem. 15 (2005) 633-648.

[80] F. Zhang, C.-H. Chen, J.C. Hanson, R.D. Robinson, I.P. Herman, S.-W. Chan, Phases in ceria-zirconia binary oxide (1-x)CeO_2-xZrO_2 nanoparticles: the effect of particle size, J. Am. Ceram. Soc. 89 (2006) 1028-1036.

[81] I. Fabregas, R.O. Fuentes, D.G. Lamas, M.E. Fernandez de Rapp, N.E. Walsoe de Reca, M.C.A Fantini, A.F. Craievich, R.J. Prado, R.P. Millen, M.L.A. Temperini, Local structure of the metal-oxygen bond in compositionally homogeneous, nanocrystalline zirconia-ceria solid solutions synthesized by a gel-combustion process, J. Phys. Condens. Matter 18 (2006) 7863-7881.

[82] M. Yashima, H. Arashi, M. Kakihana, M. Yoshimura, Raman Scattering Study of Cubic-Tetragonal Phase Transition in $Zr_{1-x}Ce_xO_2$ Solid Solution, J. Am Ceram. Soc. 77 (1994) 1067-1071.

[83] M.L. Sanjuán, P.B. Oliete, A. Várez, J. Sanz, The role of Ce reduction in the segregation of metastable phases in the ZrO_2–CeO_2 system, J. Eur. Ceram. Soc. 32 (2012) 689–696.

[84] R. Si, Y.-W. Zhang, S.-J. Li, B.-X. Lin, C.-H. Yan, Urea-Based Hydrothermally Derived Homogeneous Nanostructured $Ce_{1-x}Zr_xO_2$ (x = 0-0.8) Solid Solutions: A Strong Correlation between Oxygen Storage Capacity and Lattice Strain, J. Phys. Chem. B 108 (2004) 12481–12488.

[85] B.M. Reddy, A. Khan, Y. Yamada, T. Kobayashi, S. Loridant, J.-C. Volta, Raman and X-ray Photoelectron Spectroscopy Study of CeO_2-ZrO_2 and V_2O_5/CeO_2-ZrO_2 Catalysts, Langmuir 19 (2003) 3025-3030.

[86] R.D. Shannon, Revised effective ionic radii and systematic studies of interatomic distances in halides and chalcogenides, Acta Crystallogr. Sect. A: Cryst. Phys. Diffr. Theor. Gen. Crystallogr. 32 (1976) 751-767.

[87] T. Taniguchi, T. Watanebe, S. Ichinohe, M. Yoshimura, K.-I. Katsumata, K. Okada, N. Matsushita, Nanoscale heterogeneities in CeO_2-ZrO_2 nanocrystals highlighted by UV-resonant Raman spectroscopy, Nanoscale 2 (2010) 1426-1428.

[88] F. Zhang, C. H. Chen, J. M. Raitano, J. C. Hanson, W. A. Caliebe, S. Khalid, S. W. Chan, Phase stability in ceria-zirconia binary oxide nanoparticles: The effect of the Ce^{3+} concentration and the redox environment, J. Appl. Phys. 99 (2006) 084313.

[89] C. Andriopoulou, A. Trimpalis, K.C. Petallidou, A. Sgoura, A.M. Efstathiou, S. Boghosian, Structural and Redox Properties of $Ce_{1-x}Zr_xO_{2-\delta}$ and $Ce_{0.8}Zr_{0.15}RE_{0.05}O_{2-\delta}$ (RE: La, Nd, Pr, Y) Solids Studied by High Temperature *in Situ* Raman Spectroscopy, J. Phys. Chem. C121 (2017) 7931−7943.

[90] S. Otsuka-Yao-Matsuo, T. Omata, N. Izu, H. Kishimoto, Oxygen Release Behavior of $CeZrO_4$ Powders and Appearance of New Compounds κ and t*, J. Solid State Chem. 138 (1998) 47-54.

[91] W.H. Weber, Raman applications in catalysts for exhaust-gas treatment, in: W.H. Weber, R. Merlin (Eds.), Springer Series in Materials Science, vol.42 (Raman Scattering in Materials Science), Springer-Verlag, 2000, pp. 233-270.

[92] J.R. McBride, G.W. Graham, C.R. Peters, W.H. Weber, Growth and Characterization of reactively sputtered thin-film platinum oxides, J. Appl. Phys. 69 (1991) 1596-1604.

[93] G.W. Graham, A.E. O'Neill, D. Uy, W.H. Weber, H. Sun, X.Q. Pan, Observation of strained PdO in an aged Pd/ceria-zirconia catalyst, Catal. Lett. 79 (2002) 99-105.

[94] R.V.Gulyaev, T.Y Kardash, S.E. Malykhin, O.A. Stonkus, A.S. Ivanova, A.I. Boronin, The local structure of $Pd_xCe_{1-x}O_{2-x-\delta}$ solid solutions, Phys. Chem. Chem. Phys. 16 (2014) 13523-13539.

[95] L.S. Kibis, T.Y. Kardash, E.A. Derevyannikova, O.A. Stonkus, E.M. Slavinskaya, V.A. Svetlichnyi, A.I. Boronin, Redox and Catalytic Properties of $Rh_xCe_{1-x}O_{2-\delta}$ Solid Solution, J. Phys. Chem. C 121 (2017) 26925-26938.

[96] L.L. Murrell, S.J. Tauster, D.R. Anderson, Laser Raman Characterization of Surface Phase Precious Metal Oxides Formed on CeO_2, Stud. Surf. Sci. Catal. 71 (1991) 275-89.

[97] M.S. Brogan, T.J. Dines, J.A. Cairns, Raman spectroscopic study of the Pt-CeO_2 interaction in the Pt/Al_2O_3-CeO_2 catalyst, J. Chem. Soc. Faraday Trans. 90 (1994) 1461-1466.

[98] W. Lin, A.A. Herzing, C.J. Kiely, I.E. Wachs, Probing Metal-Support Interactions under Oxidizing and Reducing Conditions: *In Situ* Raman and Infrared Spectroscopic and Scanning Transmission Electron Microscopic-X-ray Energy-Dispersive Spectroscopic Investigation of Supported Platinum Catalysts, J. Phys. Chem. C 112 (2008) 5942-5951.

[99] J. Lee, Y.S. Ryou, X. Chan, T.J. Kim, D.H. Kim, How Pt Interacts with CeO_2 under the Reducing and Oxidizing Environments at Elevated Temperature: The Origin of Improved Thermal Stability of Pt/CeO_2 Compared to CeO_2, J. Phys. Chem. C 120 (2016) 25870-25879.

[100] Q. Wu, J. Ba, X. Yan, J. Bao, Z. Huang, S. Dou, D. Dai, T. Tang, W. Luo, D. Meng, Insight of Pt-support interaction in S-Pt/$Ce_{0.7}Zr_{0.3}O_2$ by *in situ* Raman spectroscopy, Catal. Commun. 98 (2017) 34-37.

[101] T.-S. Nguyen, G. Postole, S. Loridant, F. Bosselet, L. Burel, M. Aouine, L. Massin, P. Gelin, F. Morfin, L.Piccolo, Ultrastable iridium–ceria nanopowders synthesized in one step by solution combustion for catalytic hydrogen production, J. Mater. Chem. A 2 (2014) 19822-19832.

[102] K. Tang, W. Liu, J. Li, J. Guo, J. Zhang, S. Wang, S. Niu, Y. Yang, The Effect of Exposed Facets of Ceria to the Nickel Species in Nickel-Ceria Catalysts and Their Performance in a NO + CO Reaction, ACS Appl. Mater. Interfaces 7 (2015) 26839-26849.

[103] S. Loridant, C. Feche, N. Essayem, F. Figueras, WO_x/ZrO_2 Catalysts Prepared by Anionic Exchange: *In Situ* Raman Investigation from the Precursor Solutions to the Calcined Catalysts, J. Phys. Chem. B 2005, 109, 5631-5637.

[104] B.M. Weckhuysen, Snapshots of a working catalyst: possibilities and limitations of in situ spectroscopy in the field of heterogeneous catalysis, Chem. Commun. 2002, 97-110.

[105] M.A. Bañares, I.E. Wachs, Molecular structures of supported metal oxide catalysts under different environments, J. Raman Spectrosc. 33 (2002) 359-380.

[106] M.A. Banares, Operando methodology: combination of *in situ* spectroscopy and simultaneous activity measurements under catalytic reaction conditions, Catal. Today 100 (2005) 71-77.

[107] M.A. Banares, G. Mestl, Chapter 2 Structural Characterization of Operating Catalysts by Raman Spectroscopy, Adv. Catal. 52 (2009) 43-128.

[108] I.E. Wachs, C.A. Roberts, Monitoring surface metal oxide catalytic active sites with Raman Spectroscopy, Chem. Soc. Rev. 39 (2010) 5002-5017.

[109] M.O. Guerrero-Perez, M.A. Banares, Observing heterogeneous catalysts while they are working using *operando* Raman spectroscopy, Spectroscopy (Duluth, MN, United States) 27 (2012) 32-38.

[110] V. Calvino-Casilda, M.A. Banares, Recent advances in imaging and monitoring of heterogeneous catalysts with Raman spectroscopy, Catal. 24 (2012) 1-47.

[111] G. Mestl, M.A. Banares, Structural Characterization of Catalysts by *Operando* Raman Spectroscopy, in: J.A. Rodriguez, J.C. Hanson, P.J. Chupas (Eds.), In-situ Characterization of Heterogeneous Catalysts, John Wiley & Sons, Inc., Hoboken, 2013, pp. 267-292.

[112] I.E. Wachs, M.A Banares, *In situ* and *Operando* Raman spectroscopy of oxidation catalysts, in: D. Duprez, F. Cavani (Eds.), Advanced Processes in Oxidation Catalysis: From

Laboratory to Industry, Imperial College Press, London, 2014, pp. 420-446.
[113] G. Mestl, *In situ* Raman spectroscopy - a valuable tool to understand operating catalysts, J. Mol. Catal. A: Chem. 158 (2000) 45-65.
[114] A. Filtschew, C. Hess, Interpretation of Raman Spectra of Oxide Materials: The Relevance of Absorption Effects, J. Phys. Chem. C 121 (2017) 19280-19287
[115] J.-M. Jehng, G. Deo, B.M. Weckhuysen, I.E. Wachs, Effect of water vapor on the molecular structures of supported vanadium oxide catalysts at elevated temperatures, J. Mol. Catal. A: Chem. 110 (1996) 41-54.
[116] M.V. Bosco, M.A. Banares, M.V. Martinez-Huerta, A.L. Bonivardi, S.E. Collins, In situ FTIR and Raman study on the distribution and reactivity of surface vanadia species in V_2O_5/CeO_2 catalysts, J. Mol. Catal. A: Chem., 408 (2015) 75-84.
[117] Z. Wu, A.J. Rondinone, I.N. Ivanov, S.H. Overbury, Structure of Vanadium Oxide Supported on Ceria by Multiwavelength Raman Spectroscopy, J. Phys. Chem. C 115 (2011) 25368-25378.
[118] M.V. Martinez-Huerta, J.M. Coronado, M. Fernandez-Garcia, A. Iglesias-Juez, G. Deo, J.L.G. Fierro, M.A. Banares, Nature of the vanadia-ceria interface in V^{5+}/CeO_2 catalysts and its relevance for the solid-state reaction toward $CeVO_4$ and catalytic properties, J. Catal. 225 (2004) 240-248.
[119] M.V. Martinez-Huerta, G. Deo, J.L.G. Fierro, M.A. Banares, Changes in Ceria-Supported Vanadium Oxide Catalysts during the Oxidative Dehydrogenation of Ethane and Temperature-Programmed Treatments, J. Phys. Chem. C 111 (2007) 18708-18714.
[120] B.M. Reddy, A. Khan, Y. Yamada, T. Kobayashi, S. Loridant, J.-C. Volta, Surface Characterization of CeO_2/SiO_2 and $V_2O_5/CeO_2/SiO_2$ Catalysts by Raman, XPS, and Other Techniques, J. Phys. Chem. B 106 (2002) 10964-10972.
[121] B.M. Reddy, A. Khan, Y. Yamada, T. Kobayashi, S. Loridant, J.-C. Volta, Structural Characterization of CeO_2-TiO_2 and V_2O_5/CeO_2-TiO_2 Catalysts by Raman and XPS Techniques, J. Phys. Chem. B 107 (2003) 5162-5167.
[122] B.M. Reddy, P. Lakshmanan, S., Y. Yamada, T. Kobayashi, C. Lopez-Cartes, T.C. Rojas, A. Fernandez, Structural Characterization and Oxidative Dehydrogenation Activity of $V_2O_5/Ce_xZr_{1-x}O_2/SiO_2$ Catalysts, J. Phys. Chem. B 110 (2006) 9140-9147.
[123] M.V. Martinez-Huerta, G. Deo, J.L.G. Fierro, M.A. Banares, *Operando* Raman-GC Study on the Structure-Activity Relationships in V^{5+}/CeO_2 Catalyst for Ethane Oxidative Dehydrogenation: The Formation of $CeVO_4$, J. Phys. Chem. C 112 (2008) 11441-11447.
[124] A. Iglesias-Juez, M.V. Martinez-Huerta, E. Rojas-Garcia, J.-M. Jehng, M.A. Banares,

Nature of unusual redox cycle at vanadia ceria interface, J. Phys. Chem. C 122 (2018) 1197-1205.

[125] Z. Wu, M. Li, S.H. Overbury, Raman Spectroscopic Study of the Speciation of Vanadia Supported on Ceria Nanocrystals with Defined Surface Planes, ChemCatChem 4 (2012) 1653-1661.

[126] Y.M. Choi, H. Abernathy, H.-T. Chen, M.C. Lin, M. Liu, Characterization of O_2−CeO_2 Interactions Using *in Situ* Raman Spectroscopy and First-Principle Calculations, ChemPhysChem 7 (2006) 1957−1963.

[127] Y. Zhao, B.-T. Teng, X.-D. Wen, Y. Zhao, Q.-P. Chen, L.-H. Zhao,M.-F. Luo, Superoxide and Peroxide Species on CeO_2(111), and Their Oxidation Roles. J. Phys. Chem. C 116 (2012) 15986−15991.

[128] M. Huang, S. Fabris, Role of Surface Peroxo and Superoxo Species in the Low-Temperature Oxygen Buffering of Ceria: Density Functional Theory Calculations, Phys. Rev. B: Condens. Matter Mater. Phys. 75 (2007) 081404.

[129] C. Schilling, M.V. Ganduglia-Pirovano, C. Hess, Christian, Experimental and Theoretical Study on the Nature of Adsorbed Oxygen Species on Shaped Ceria Nanoparticles, J. Phys. Chem. Letters 9 (2018) 6593-6598.

[130] M. Lohrenscheit, C. Hess, Direct Evidence for the Participation of Oxygen Vacancies in the Oxidation of Carbon Monoxide over Ceria-Supported Gold Catalysts by Using *Operando* Raman Spectroscopy, ChemCatChem 8 (2016) 523−526.

[131] C. Schilling, C. Hess, Elucidating the Role of Support Oxygen in the Water-Gas Shift Reaction over Ceria-Supported Gold Catalysts Using *Operando* Spectroscopy, ACS Catal. 9 (2019) 1159-1171.

[132] Ph. Colomban, G. Gouadec, Raman and IR micro-analysis of high performance polymer fibres tested in traction and compression, Composites Science and Technology 69 (2009) 10-16.

[133] Ph. Colomban, Proton and Protonic Species: The Hidden Face of Solid State Chemistry. How to Measure H-Content in Materials? Fuel Cell 13 (2013) 6-18.

[134] A. Filtschew, D. Stranz, C. Hess, Mechanism of NO_2 storage in ceria studied using combined *in situ* Raman/FT-IR spectroscopy, Phys. Chem. Chem. Phys. 15 (2013) 9066-9069.

[135] A. Filtschew, C. Hess, Unravelling the mechanism of NO and NO_2 storage in ceria: The role of defects and Ce-O surface sites, Appl. Catal. B: Environmental 237 (2018) 1066-1081.

[136] P. Michalowski, A. Gräfenstein, M. Knipper, T. Plaggenborg, J. Schwenzel, J. Parisi,

Examining Inhomogeneous Degradation of Graphite/Carbon Black Composite Electrodes in Li-Ion Batteries by Lock-In Thermography, J. Electrochem. Soc. 164 (2017) A2251-A2255.
[137] M. Toledano, R. Osorio, E. Osorio, F. Garcıa-Godoy, M. Toledano-Osorio, F.S. Aguilera, Advanced zinc-doped adhesives for high performance at the resin-carious dentin interface, Journal of the Mechanical Behavior of Biomedical Materials, 62 (2016) 247–267.
[138] M.W. Zandbergen, S.D.M. Jacques, B.M. Weckhuysen, A.M. Beale, Chemical Probing within Catalyst Bodies by Diagonal Offset Raman Spectroscopy, Angew. Chem. Int. Ed. 51 (2012) 957 –960.
[139] K.D.M. Harris, Explorations in the Dynamics of Crystalline Solids and the Evolution of Crystal Formation Processes, Isr. J. Chem. 57 (2017) 154 –170.
[140] F. Tres, K. Treacher, J. Booth, L.P. Hughes, S.A.C. Wren, J.W. Aylott, J.C. Burley, Real time Raman imaging to understand dissolution performance of amorphous solid dispersions, J. Control. Release 188 (2014) 53–60.
[141] H. Kim, K.M. Kosuda, R.P. Van Duyne, P.C. Stair, Resonance Raman and surface- and tip-enhanced Raman spectroscopy methods to study solid catalysts and heterogeneous catalytic reactions, Chem. Soc. Rev. 39 (2010) 4820-4844.
[142] T. Schmid, L. Opilik, C. Blum, R. Zenobi, Nanoscale Chemical Imaging Using Tip-Enhanced Raman Spectroscopy: A Critical Review, Angew. Chem. Int. Ed. 52 (2013) 5940-5954.
[143] T. Hartman, C.S. Wondergem, N. Kumar, A. van den Berg, B.M. Weckhuysen, Surface- and Tip-Enhanced Raman Spectroscopy in Catalysis, J. Phys. Chem. Lett. 7 (2016) 1570-1584.
[144] N. Kumar, B. Stephanidis, R. Zenobi, A. J. Wain, D. Roy, Nanoscale mapping of catalytic activity using tip-enhanced Raman spectroscopy, Nanoscale, 7 (2015) 7133–7137.
[145] N.M. Ralbovsky, I.K. Lednev, Raman spectroscopy and chemometrics: A potential universal method for diagnosing cancer, Spectroc. Acta A 219 (2019) 463-487.
[146] J. Yang, J. Xu, X. Zhang, C. Wu, T. Lin, Y. Ying, Deep learning for vibrational spectral analysis: Recent progress and a practical guide, Anal. Chim. Acta 1081 (2019) 6-17.
[147] R. Deidda, P.-Y Sacre, M. Clavaud, L. Coic, H. Avohou, P. Hubert, E. Ziemons, Vibrational spectroscopy in analysis of pharmaceuticals: Critical review of innovative portable and handheld NIR and Raman spectrophotometers, Trends Anal. Chem. TrAC 114 (2019) 251-259.
[148] S.J. Mazivila, A.C. Olivieri, Chemometrics coupled to vibrational spectroscopy and spectroscopic imaging for the analysis of solid-phase pharmaceutical products: A brief review

on non-destructive analytical methods, Trends Anal. Chem. TrAC 108 (2018) 74-87.

Caption for figures

Figure 1. (a) Raman spectra of single crystal and nanocrystalline CeO_2 together with the curve fit according to the spatial correlation model (b) Correlation length as a function of crystallite size of nanocrystalline CeO_2 thin films. The dashed line is the correlation length estimated from a spherical model [28].

Figure 2. (a) Absorption spectrum and (b) UV/vis Raman spectra of ceria sample annealed at 1000 °C (crystallite size: 82.2 nm). Reprinted with permission from [42] Copyright 2009 American Chemical Society.

Figure 3. Raman spectra of Pt/CeO_2 catalysts recorded in the 1900-2400 cm^{-1} spectral ranges at RT after the initial oxidizing pre-treatment at 500 °C under 20% O_2 flow for 1 h and after successive reductions (Red1, 2 and 3) at 250 °C in H_2-N_2 and re-oxidations (Reox1, 2 and 3) at 250 °C in O_2-He.

Figure 4. Raman spectra of CeO_2 collected at room temperature after calcination at 673 K, H_2 treatment at 533, 623, and 673 K, and exposure to O_2 at room temperature. The Raman peak marked with an asterisk (*) represents a laser plasma line and was used to normalize the Raman spectra intensity. Reprinted with permission from Ref. [60] Copyright 2017 American Chemical Society.

Figure 5. Raman spectra of $Ce_{0.8}Pr_{0.2}O_{2-\delta}$ recorded after reduction at 800 K for 60 min under 10% H_2 flow at (a) 77 K and after oxidation at 800 K for 30 min under 5% O_2 flow (b) at 77 K, (c) at 163 K, and (d) at 298 K using λ = 514 nm and P = 103 μW. The inset corresponds to a zoom of figures (a) and (b) between 300 and 700 cm^{-1} (Adapted from [72]).

Figure 6. (a) Raman spectra of (a) as-prepared and (b) calcined at 1173 K $Ce_{(1-x)}Zr_xO_2$ (x = 0-0.8) samples. Reprinted with permission from Ref. [84] Copyright 2004 American Chemical Society.

Figure 7. In situ Raman spectra of (a) 2 wt%Pt/CeO_2 calcined at 500 °C (labelled $Pt(2)/CeO_2$ 500C) and (b) 2 wt%Pt/CeO_2 calcined at 800 °C (labelled $Pt(2)/CeO_2$ 800C) recorded at temperature from 50 to 250 ° C with a temperature step of 25 °C, under 3% H_2/Ar. The

parentheses value is the wt% of Pt in the sample. Each temperature was maintained for 20 min, and Raman spectra were obtained after cooling down to 50 °C. Reprinted with permission from [99] Copyright 2004 American Chemical Society.

Figure 8. Visible (A) and UV (B) Raman spectra of dehydrated VO_x/r-CeO_2 (CeO_2 nanorods) and VO_x/c-CeO_2 (CeO_2 nanocubes) samples as a function of surface VOx density (V nm^{-2}). The inset in parts B is a plot of the ratio of I_D/IF_{2g} versus the surface VOx density. * indicates a plasma line from the laser. Reprinted with permission from Ref. [125] Copyright 2012 Wiley-VCH Verlag GmbH& Co. KGaA, Weinheim.

Figure 9. Comparison of the Raman spectra of pristine CeO_2 and 0.7% Pt/CeO_2 catalyst after reduction at 400, 450, and 500 °C recorded at -100 °C under O_2 flow.

Figure 10. Raman spectra of bare CeO_2 at 120 °C during exposure to WGS reaction conditions (left panel: 2% CO, 8% $H_2{}^{18}O$, orange; right panel: 2% CO, 8% $H_2{}^{16}O$, red). For comparison, spectra in argon (black), in 8% $H_2{}^{18}O$ (dark blue left panel), and in 8% $H_2{}^{16}O$ (blue right panel) are shown. Spectra are offset for clarity. Reprinted with permission from Ref. [131] Copyright 2018 American Chemical Society.

Figure 11. *In situ/operando* Raman spectra (phonon region) of 0.5 wt % Au/CeO_2 at 120 °C exposed to argon (black), WGS reaction conditions (2% CO, 8% $H_2{}^{16}O$, red), WGS reaction conditions (2% CO, 8% $H_2{}^{18}O$, orange), 10% $H_2{}^{16}O$ (blue), 8% $H_2{}^{18}O$, (dark blue), 2% CO (green), and CO oxidation reaction conditions (2% CO, 10% O_2, brown). Prior to all in situ measurements, the catalyst was equilibrated in argon at 120 °C. The F2g band is cut off, and the position of the F_{2g} band is given at the right of the panel. Spectra are offset for clarity. Reprinted with permission from Ref. [131] Copyright 2018 American Chemical Society.

Figure 12. (a) *In situ* Raman spectra of oxidatively treated ceria showing the temporal evolution upon exposure to 500 ppm NO_2/20% O_2/N_2 at 30 °C An enlarged view of the Raman spectra is shown for the regions (b) 200–700 cm^{-1}, (c) 500–1800 cm^{-1}, and (d) 3000–4000 cm^{-1}. Reprinted with permission from Ref. [135] Copyright 2018 Elsevier B.V. All rights reserved.